3D Bioprinting of Nanoparticle Incorporated Cell-Laden Bioink for Muscle Tissue Engineering

Sami Şanlıdağ

Master's Thesis

Åbo Akademi University
Faculty of Science and Engineering
26.05.2019

Master's Degree in Biomedical Imaging
Regenerative Medicine

Credits: 40 ECTS

Supervisor:
Prof. Jessica Rosenholm, Pharmaceutical Sciences Laboratory, Åbo Akademi University

Examiners:
1: Prof. Jessica Rosenholm
2: Prof. Cecilia Sahlgren

ÅBO AKADEMI UNIVERSITY
Faculty of Science and Engineering

Sami ŞANLIDAĞ: 3D Bioprinting of Nanoparticle Incorporated Cell-Laden-Bioink for Muscle Tissue Engineering

Master's Thesis, 53 pp., II Appendices
Regenerative Medicine
April 2019

ABSTRACT

Tissue engineering has emerged as a promising field to restore large volumetric muscle loss. However, due to its highly dynamic niche, myogenesis is rather complex. Thus, development of biocompatible bioinks with intracellular drug delivery mechanisms to control biological cues in the cell niche is necessary to construct scaffolds and, guide myogenesis. In this study, we aimed to formulate a gelatine methacrylate (GelMA) and nanofibrillated cellulose (NFC) composite cell-laden bioink, and optimize its bioprinting process using C2C12 myoblasts. We also aimed to select the most suitable surface modification for the MSNs for uniform dispersion, high cellular internalization and low cytotoxicity to incorporate them into the bioink, with the prospect of loading them with suitable drugs to show their further use to control cell differentiation. The NFC/GelMA bioink showed excellent printability, and high structural fidelity. However, it showed high stiffness compared to the native skeletal muscle tissue. Based on the confocal microscopy and the viability quantization over a 7-day culture period, a slow cellular attachment and a viability of 15% was achieved. Furthermore, the MSNs showed time-dependent toxicity in the composite matrix. Among the MSNs with different surface modifications used, the negatively charged MSNs showed the most uniform distribution in the composite matrix. They also facilitated a slightly higher viability compared to the other nanoparticles, and showed intracellular drug delivery ability. With this work, we developed a new approach to elucidate the MSN behaviour in 3D matrices, and paved the way for the development of potential advanced scaffolds for muscle tissue engineering.

KEYWORDS: Bioprinting, mesoporous silica nanoparticles, tissue engineering

LIST OF ABBREVIATIONS

3D Printing: Three-dimensional printing

ACA: Acetic anhydride

APS: ammonium persulfate

APTES:(3-Aminopropyl) triethoxysilane

EBB: Extrusion-based bioprinting

ECM: Extracellular matrix

CTAB: cetyltrimethylammonium bromide

DiD:1,1'-Dioctadecyl-3,3,3',3'-Tetramethylindodicarbocyanine (fluorophore)

GelMA: Gelatine methacrylate

hMSCs: human mesenchymal stem cells

hyaMA: methacrylated hyaluronan

LAP: Lithium phenyl(2,4,6-trimethylbenzoyl) phosphinate

MSN: Mesoporous silica nanoparticles

NFC: Nanofibrillated cellulose

PEI: Polyethylene imine

PEG: Polyethylene glycol

PLA: Polylactic acid

PFA: Paraformaldehyde

SEM: Scanned electron microscopy

SUCC: Succinic anhydride

TEM: Transmission electron microscopy

TEMED: Tetramethylethylenediamine

TEOS: Tetraethyl orthosilicate

TMB:3,3',5,5'-Tetramethylbenzidine

TRITC: Tetramethylrodamine isothiocyanate (fluorophore)

CONTENTS

1) INTRODUCTION

Tissue engineering practices mainly focus on substituting the dysfunctional tissue with an artificial graft or promoting the regeneration in the damaged area with the aid of understanding and intersection of several fields, such as materials science and cell biology. Over the past two decades, tissue engineering has initially emerged as an alternative and sustainable area of research in regenerative medicine, in response to the limitations in organ transplantation practices (Furth and Atala, 2014). Organ transplantations have been the major treatment strategy for the damaged or dysfunctional tissues and organs. However, the number of organ donations do not cater to the growing need for organs. Furthermore, clinical problems, such as donor-recipient mismatch that causes immune rejection of the transplanted organ, immensely impact the success of the organ transplantations (Ingulli, 2010). On the other hand, tissue engineering uses the

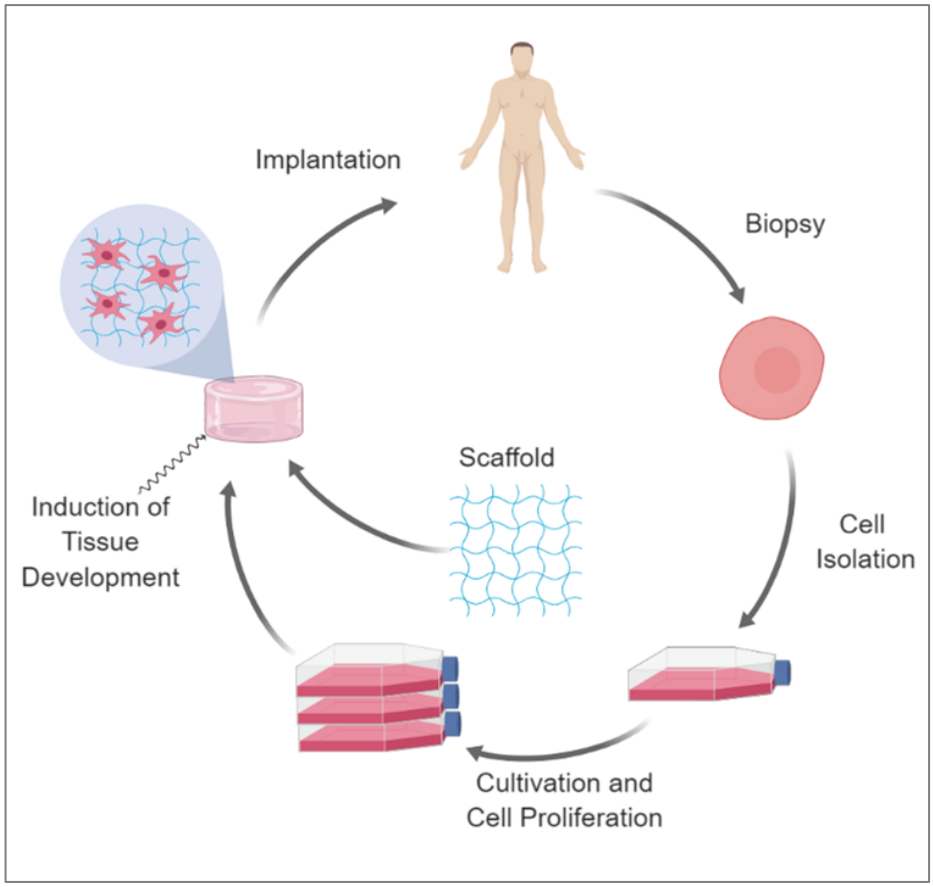

Figure 1) *In vitro* tissue engineering: *In vitro* tissue engineering aims at restoring damaged tissues by inducing proliferation and differentiation of patient derived stem cells in porous scaffolds to produce tissue grafts (Adapted from Killian et al, 2012).

patient-derived stem cells to construct new tissue *in situ* or *in vitro,* thereby avoiding immune rejection. *In situ* tissue engineering approach mainly focuses on encouragement of stem cell differentiation and tissue development at the targeted site of the body by employing biomaterials and biological cues (Sengupta et al., 2014). *In vitro* tissue engineering approach to restoring the damaged tissue involves the cultivation of patient-derived stem cells in porous constructs called scaffolds, induction of cell differentiation and tissue development. Afterwards, the tissue construct is implanted to the patient (**Figure 1**) (Killian et al., 2012). *In vitro* tissue engineering approach offers high control and easier tracking of the tissue development. Furthermore, it has recently drawn growing attention a potential sustainable drug screening model (Rouwkema et al., 2011; Sengupta et al., 2014).

1.1) Muscle Restoration and Muscle Tissue Engineering

Constituting 60% of the whole body, skeletal muscle is the most abundant tissue in the human body and is responsible for mobility (Vigodarzere, 2014). Therefore, the loss or dysfunction of muscle tissue can be catastrophic. Muscle dystrophy, a genetical disorder that causes progressive weakness and destruction of muscle tissue is responsible for large volumetric losses of muscle tissue resulting in loss of mobility and eventually death in early ages (Leung and Wagner, 2013). Even though muscle tissue possesses high self-regeneration potential, surgical intervention is required in such extreme cases of muscle losses that are over the critical point (Arab, 2018). Autografting, implantation of the muscle tissue taken from the patient's healthy muscle tissue to the damaged area, has been the conventional clinical approach to restore muscle loss (Zorlutuna et al, 2012). On the other hand, in the case of muscle dystrophy, the patients already lack the healthy tissue, and thus the potential of autografting as a treatment is limited. Therefore, there has been a growing need for alternative methodologies to replace or restore the muscle damage/loss. At this point, muscle tissue engineering emerges as a promising approach. However, engineering and fabricating muscle tissue with well-organized muscle fibre geometry, which involves several biochemical and biomechanical processes, is rather complex due to the highly dynamic nature of myogenesis (Vigodarzere, 2014).

1.2) Skeletal Muscle Stem Cells

Naturally, the selection of the cell source for tissue engineering has been a major criterion and starting point for muscle tissue engineering. Stem cells have been promising cell sources in this context, thanks to their high potency of self-renewal and high proliferation rate and their ability to differentiate into one or multiple different cell lineages based on their differentiation potential (Bacakova et al., 2018). However, stem cell nature is rather complex and mostly genetically-driven. Therefore, controlling the parameters affecting the stem cell mechanics has been a major obstacle. In addition, epigenetic factors, such as signals received from the micro-milieu, highly affect the stem cell proliferation, migration and differentiation. (Lin et al., 2018)

Muscle stem cells or satellite cells occur in a quiescent state in the basal lamina of mature skeletal muscle fibres, and they are responsible for the regeneration of the tissue. In case of damage, satellite cells first differentiate into myoblasts, which proliferate and fuse to form multinucleated myotubes. Myotubes then align and form mature muscle fibre bundles (**Figure 1.2**) (Enwere, et al., 2014). For muscle tissue engineering studies, myoblasts emerge as a potential cell source thanks to their high proliferation and commitment to myogenic fate (Somers et al., 2017). However, control of myoblast fusion and myotube alignment are crucial to facilitate *in vitro* muscle bundle formation. Up to date, researchers reported many factors that lead to myoblast fusion, such as Notch inhibition (Buas and Kadesch, 2010), mechanical stress (Vandenburgh et al., 2008),

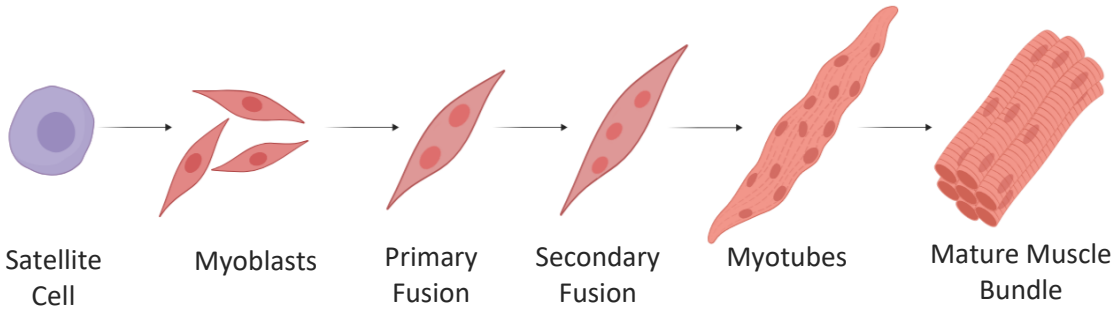

Figure 1.2) Skeletal muscle myogenesis: In case of damage, satellite cells first differentiate into myoblasts, which proliferate and fuse to form multinucleated myotubes. Myotubes then align and form mature muscle bundles (Adapted from Enwere et al, 2014).

biomaterial stiffness (Romanazzo et al., 2012) and voltage difference across the cell media (Laternser et al., 2018).

1.3) Stem Cell Niche and Tissue Engineering Scaffolds

Stem cell niche refers to the dynamic complex milieu that not only encompasses the stem cells. It comprises of extracellular matrix (ECM), other cells, signalling molecules, metabolic and immunological components as well as the mechanical and topographical factors (Lane et al., 2014).

One of the major components of stem cell niche, ECM is defined as 3D networks of polysaccharides and proteins that surrounds *in vivo* cells. It serves not only as an attachment site for the cells but also influences their function and fate (Florczyk, 2017). In the case of tissue engineering, ECM is constituted by synthetically constructed scaffolds. Tissue engineering scaffolds are 3D porous constructs that are made of biomaterials. They serve as attachment surfaces for the cells, guide the formation of the neo-tissue, and provide mechanical support (Lane et al., 2014; Rosenholm et al., 2016). An ideal scaffold is highly biocompatible, biodegradable, and physically durable; and has similar architecture and suitable mechanical properties with native ECM (O'Brien, 2011). Among these properties, stiffness of the scaffold, a mechanical property, is a major concern in biomaterial selection having a direct impact on differentiation. Each animal tissue shows different mechanical characteristics and possesses different stiffness values. For example, brain is characterized by a stiffness between 0.1 to 1 kPa, whereas this value for skeletal muscle is 8-17 kPa. Therefore, the stiffness of the scaffold must match that of the native tissue to create a similar niche for the precise control of the tissue architecture (Engler, 2006).

In this regard, hydrogels emerge as ideal candidates as scaffold materials for engineering soft tissues thanks to their suitable range of stiffness. Furthermore, they offer high biocompatibility, porous structure and mechanical tunability as printable scaffold materials. Hydrogels are defined as 3D meshes of hydrophilic polymers, which are either chemically or physically crosslinked, and are able to hold high amount of water. (Shin et al., 2017; El-Sherbiny and Yacoub, 2016). They are classified under two groups based on their origin as synthetic and natural hydrogels (Ahmed, 2015). A brief explanation of

advantages and disadvantages of synthetic and natural polymers are given in **Table 1.3**. Synthetic polymers, such as polyethylene glycol (PEG) and poly lactic acid (PLA), are often used as hydrogel biomaterials due to their highly tuneable nature and reproducibility. On the other hand, hydrogels with natural origins, such as collagen, hyaluronic acid, alginate and gelatine methacrylate (GelMA) offer high biocompatibility due to their characteristics, such as biological recognition, low immunological response and low cytotoxicity (Zhao et al., 2012; El Sherbiny and Yacoub 2016; Nichol et al., 2010).

Table 1.3) A comparison of the polymers based on their origins: Advantages and disadvantages of natural and synthetic polymers. (E. Özliseli, Personal Communication).

	Examples	Advantages	Disadvantages
Natural polymers	Chitosan, alginate, collagen,silk hyaluronic acid, albumin, gelatin, fibrinogen, silk	Low immunorejection Provides binding sites	Batch-to-batch changes Potential impurities Limited mechanical properties
Synthetic polymers	poly (lactic-co-glycolic acid) (PLGA), polycaprolactones (PCL), polyacrylates (PCA), polylactide	Pure Tunable mechanical properties	Immunorejection risk

Furthermore, combining the attractive properties of multiple single-phase hydrogels, composite hydrogels has drawn growing attention in tissue engineering research as tailorable scaffold materials. By changing the composition of hydrogel components in composite hydrogels, mechanical, topographical and biological properties of the scaffolds can be tuned to mimic the hierarchical architecture of native tissue (Sheffield et al., 2018). In this study, nanofibrillated natural-origin cellulose/gelatine methacrylate (NFC/GelMA) composite hydrogels were used as bioink formulations to achieve high biocompatibility and similar mechanical properties those of soft tissues. More thorough information regarding NFC and GelMA are given below.

1.3.1) Gelatine Methacrylate (GelMA)

Among the natural polymers used for tissue engineering, gelatine methacrylate (GelMA) has been one of the most commonly used hydrogels. GelMA is a photopolymerizable form of gelatine prepared by addition of methacrylate groups to the amine-containing side groups, which polymerize under UV light irradiation in the presence of a photo-initiator (**Figure 1.3.1**). The cross-linking density of GelMA can be tuned by changing the UV

irradiation time to adjust its mechanical properties. With its high ability to mimic the ECM components and durability at 37 ºC, GelMA is designated to be a promising scaffold component for tissue engineering (Nichol et al., 2010). In addition, it facilitates high cellular viability and attachment and thus is highly biocompatible. GelMA is mainly used as a bioink component for 3D printing (Wang, 2017). However, it can also be used as auxiliary material to facilitate the printing of other hydrogels (Xu, 2019). In this study GelMA was used as an auxiliary material to tune the printability of NFC, and to provide biological recognition sites for cellular attachment and growth.

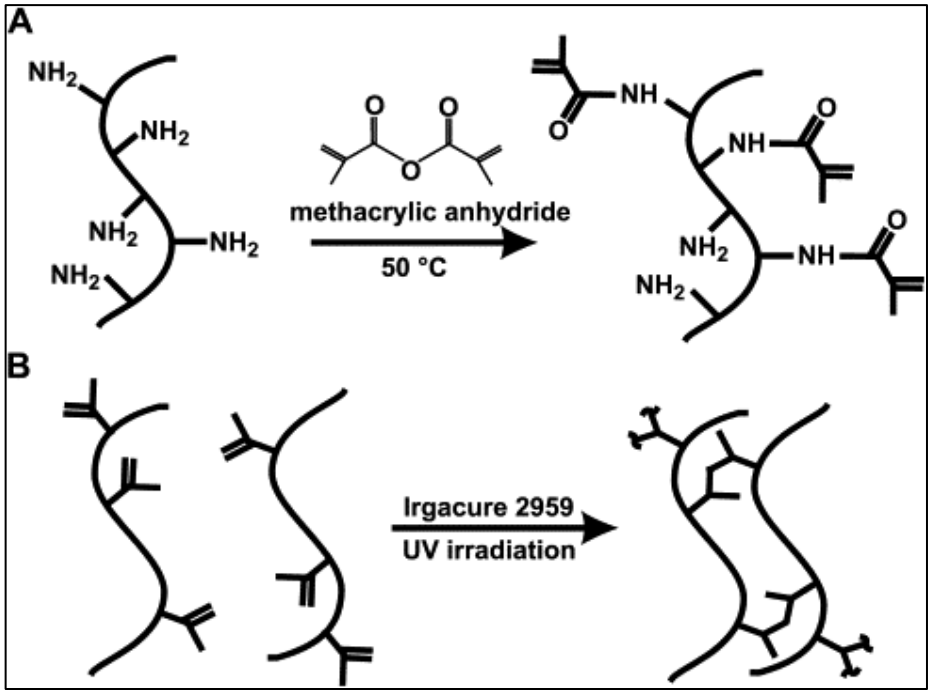

Figure 1.3.1) GelMA as a photo-crosslinkable hydrogel: Synthesis of gelatine methacrylate (GelMA) and its photo-crosslinking by using Irgacure 2959 and UV irradiation (365 nm) (Nichol et al., 2010, reprinted with the permission of the copyright

1.3.2) Nanofibrillated Cellulose (NFC)

Cellulose being the most abundant polymer in nature, nanofibrillated cellulose (NFC), a wood-based hydrogel, have gained interest in tissue engineering research as a potential biomaterial for 3D cell cultures. Due to the strong hydrogen bonding of water molecules to the hydroxyl groups of the cellulose fibres, NFC possesses high water retention capability, and thus high similarity to soft tissue in terms of the mechanical properties. (Shin et al., 2017; Laurén, 2018). NFC is rich in finely structured fibres, and is considered

to be non-toxic. Therefore, it resembles the native ECM components and has a positive effect on cell fate (Ávila et al., 2017).

NFC is produced in mechanical ways by disintegrating larger cellulose bundles to smaller fibrils that have a width less than 100 nm and varying lengths (Chinga-Carrasco, 2011; Alexandrescu et al., 2013). In addition, NFC offers a possibility of a wide range of chemical modifications, thanks to its abundance of hydroxyl groups (Laurén, 2018). For example, 2,2,6,6-tetramethylpipelidine-1-oxyl (TEMPO)-mediated oxidation is used to introduce more aldehyde and carboxylic groups onto the NFC surface, which facilitate a high density of negative surface charges for the adsorption of biomolecules (Weishaupt et al., 2015).

Traditional strategies to prepare hydrogel scaffolds, such as mould-casting, mainly focus on obtaining substrates with simple geometries. However, 3D printing avails the fabrication of scaffolds in controlled geometries (Negrini et al., 2018). In this regard, in addition to its structural and chemical tunability as a 3D cell culture substrate, NFC naturally possesses shear thinning properties and shows thixotropic behaviour; thus, it is considered as an outstanding bioink material for 3D bioprinting (Hubbe et al., 2017). However, it still leaves room for improvement in terms of its printability and post-printing fidelity. In this regard, NFC can be blended with gelatine methacrylate (GelMA) as an auxiliary material to tailor its mechanical properties and printability. After blended with NFC, GelMA is 3D-printed and subjected to light irradiation to easily photo-induce a chemical crosslinking between the collagen fibres, whereas the cellulose nanofibres are physically cross-linked and entrapped by GelMA matrix to mimic the native ECM (Xu et al., 2018).

1.4) 3D Bioprinting Technology

Three-dimensional printing is a promising approach to construct cell-laden constructs with well-defined geometry. The most common 3D bioprinting modalities are inkjet bioprinting, orifice-free bioprinting and extrusion-based bioprinting (EBB). Among these, EBB stands out as a convenient layer-by-layer printing technique that avails 3D bioprinting of cell-laden bioinks with high cell concentration ($>10^6$ cell/ml) and high viscosity (**Figure 1.4**). In contrast to the other two modalities which dispense droplets, EBB dispenses hydrogel bioinks directly as fibres. Also, multiple printing nozzles can be used during the EBB process, allowing usage of multiple hydrogels at the same time to

achieve more complex structures. After the desired structure of the tissue is defined with computer-aided design (CAD) software, the tissue construct can be printed with EBB approach (Hölzl et al., 2016; You et al., 2017).

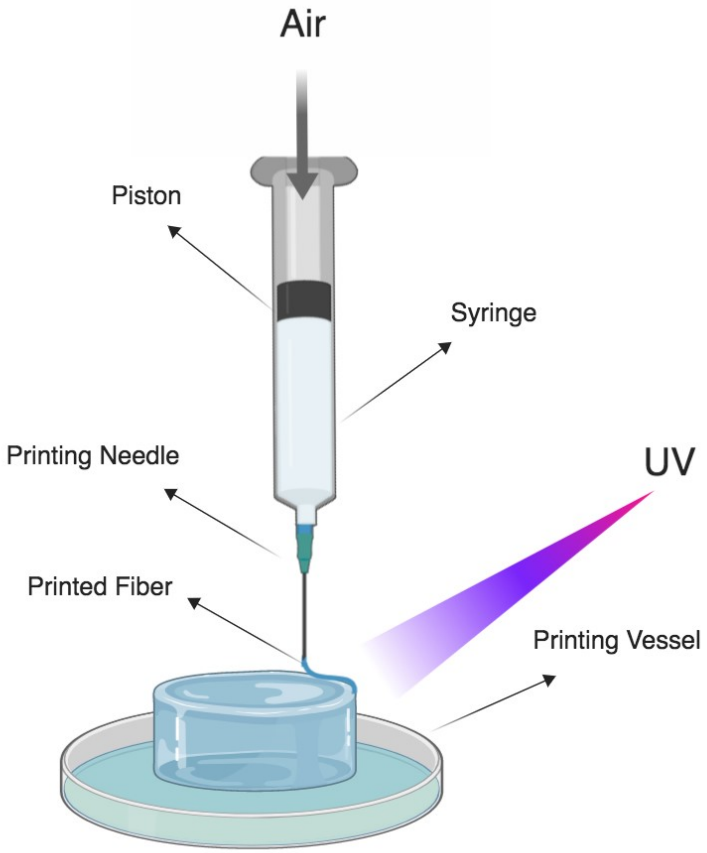

Figure 1.4) Schematic description of the working principle of extrusion-based bioprinters (EBB): EBB printers dispense bioink as fibres to construct structures well-defined geometries, and can be coupled with a UV source for photo-crosslinking (Adapted from You et al., 2017).

1.5) Design Criteria for 3D Printable Bioinks

When formulating a bioink for 3D bioprinting, a few criteria should be taken into consideration. Some of these criteria are given below.

Viscosity; viscosity refers to the resistance of a fluid to flow. Sufficient viscosity is crucial for the printed bioink strands to maintain their cylindrical shape. However, highly viscous bioinks require high pressure for extrusion through the printer nozzle resulting in high

shear force, and thus possible damage on cell morphology. Owing to their high molecular weight, natural polymers offer sufficient viscosity at low concentrations and also higher efficiency of cell encapsulation and thus proliferation and migration rate (You et al., 2017; Kyle et al., 2017).

Shear Thinning; shear thinning refers to the decrease in viscosity as the shear rate increases. Shear thinning is significant in the polymer solutions with high concentrations. When exerted through the nozzle, polymer hydrogels exhibit shear thinning resulting in a decrease both in viscosity and shear stress, and thus increased cell viability in 3D printed constructs. Also, after the bioink is exerted, the shear rate decreases significantly whereas the viscosity increases, which favour the structural integrity (Hubbe et al., 2017; You et al, 2017)

Biocompatibility; in order to achieve high cell viability, biomaterials that are used in the manufacture of the bioink must possess low cytotoxicity, be non-immunogenic and not release toxic by-products as a result of the degradation process. In the bioprinting context, the entire bioprinting process must be biocompatible to be able to avoid causing stress on the cells as much as possible (Merceron and Murphy, 2015).

Printability; in the context of bioprinting, printability refers to the capability of a bioink to be printed as initially designed and maintain the printed structure. It is affected by viscosity, cross-linking mechanisms, surface tension and other rheological characteristics of the bioink material (Kyle et al., 2017).

Cross-linking Mechanisms; highly viscous cell-laden polymer-based bioinks possess high printability. However, the high viscosity has a negative impact on cell viability. Therefore, instead of preparing a bioink with high viscosity, the bioink is desired to have sufficient viscosity and cross-link rapidly after the printing to achieve high fidelity of the printed structure. The photo-induced cross-linking mechanism is one of the promising approaches in the field (You et al., 2017).

1.6) Mesoporous Silica Nanoparticles (MSNs) for the Control of Myogenesis

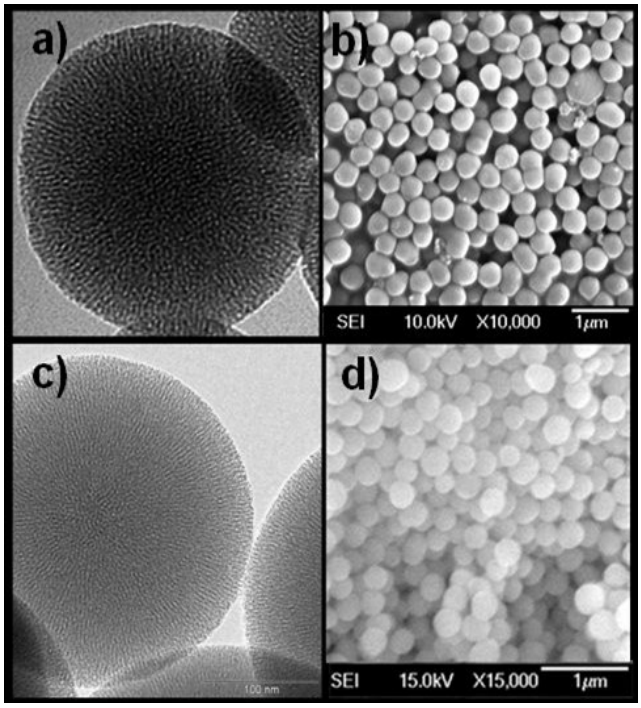

Figure 1.6.a) Electron microscopy images of spherical mesoporous silica nanoparticles: a,c) TEM image b,d) SEM images corresponding to a and c (Desai et al., 2014, reprinted with the permission of the copyright holder).

As discussed earlier, stem cell-material interactions and stem cell niche play an important role in stem cell fate, and thus are of high importance for the success of tissue engineering research. The mechanical and topographical aspect of such interactions can be addressed with the selection and fabrication of the correct biomaterials. However, biological signalling and other components of the stem cell niche are rather complex, yet crucial for stem cell differentiation, even though they are mostly overlooked (Rosenholm et al., 2016). Mesoporous Silica Nanoparticles (MSNs) are considered to be promising tools in regenerative medicine as vectors of targeting and controlled release of drugs, which in the case of tissue engineering can be utilized to control biological cues and mediate the cell proliferation, alignment and differentiation (Kim et al., 2014; Mamaeva et al., 2011).

MSNs have emerged as a suitable nano cargo delivery tools due to their tuneable pore size, low toxicity, high drug loading capacity, attachment of targeting moieties and straightforward synthesis. MSNs are characterized by a uniform and adjustable pore size between 2-50 nm (**Figure 1.6.a**). Sol-gel methodology is the common strategy to synthesize MSNs, which is performed by building a SiO_2 structure around surfactant micelles using a silica precursor, followed by the removal of the micelles (e.g. by

calcination or solvent extraction) to create pores within the silica matrix (**Figure 1.6.b**) (Vazquez, 2017).

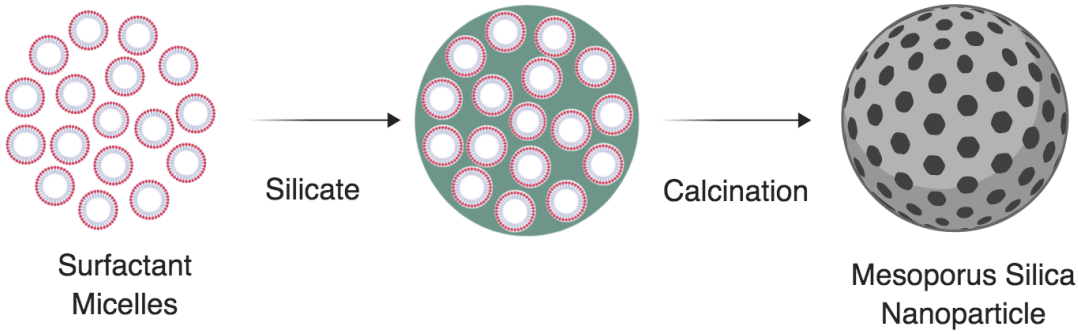

Figure 1.6.b) Schematic description of sol-gel synthesis of mesoporous silica nanoparticles (MSNs): Using a silica precursor, a SiO_2 structure is built around surfactant micelles, which are then calcinated to create pores inside the silica matrix.

1.6.1) Surface Functionalization of MSNs

As versatile drug delivery tools, MSNs can be modified with different polymers and other organic functional groups in order to tailor their properties, such as their surface properties and optical properties (Desai et al., 2014). The functionalization can be done either directly during the synthesis by co-condensation, or by post-synthetic modification. Co-condensation is widely used for fluorescent labelling of the nanoparticles by incorporating fluorophores inside the silica matrix, thus availing their optical tracking inside the physiological environment. By co-condensation, the pore walls can also be functionalized and tuned for the loading and the delivery of the drug of interest. On the other hand, post-synthetic modifications are used to tune the surface properties of MSNs, whereas maintaining the original structure of the particles (Stein et al., 2000; Hoffmann et al., 2006; Yang et al., 2012). During post-synthetic modification, surface silanol groups serve as anchoring moieties for covalent binding of the functional groups. Therefore, the number of surface silanol groups is a key parameter that determines the coverage of the MSN with the organic functional groups or polymers. However, surface silanol groups can be grafted with hyper branched polymers, such as hyper branched polyethylene imine (PEI), to create more anchoring sites, i.e. for secondary coating (**Figure 1.6.1**) (Kim et al., 2003). For example, PEI coating leads to a highly positive surface charge for MSNs,

and thus redounds to their dispersibility and stability in physiological environment (Kim et al., 2003). The high positive charge of PEI-coated particles also facilitates increased cellular internalization, as the cell membrane is negatively charged. However, the high amount of positive surface charge and high molecular weight of PEI in free form destabilize the cell membrane, and ultimately cause cell death (Kim et al., 2015; Zhang et al., 2014). Such cytotoxic effect of PEI can be minimized by derivatization, by adding a secondary layer of a different polymer or surface functional group. Derivatization of PEI results in different surface charge, and thus avails a control over the MSNs fate and impact in the physiological environment. For example, succinic anhydride derivatization (SUCC) is used to change the amino groups with carboxyl groups, which yield in highly negative surface charge. Acetic anhydrite capping (ACA), on the other hand, results in a surface charge within neutral range (Rosenholm et al., 2008; Desai, 2016). Hydrophilicity of MSN-PEI can also be tuned with a secondary coating, such as polyethylene glycol (PEG), which reduces the protein adsorption around the nanoparticle, availing immune evasion and stealth in addition to a surface charge in the neutral range (Jokerst et al., 2011).

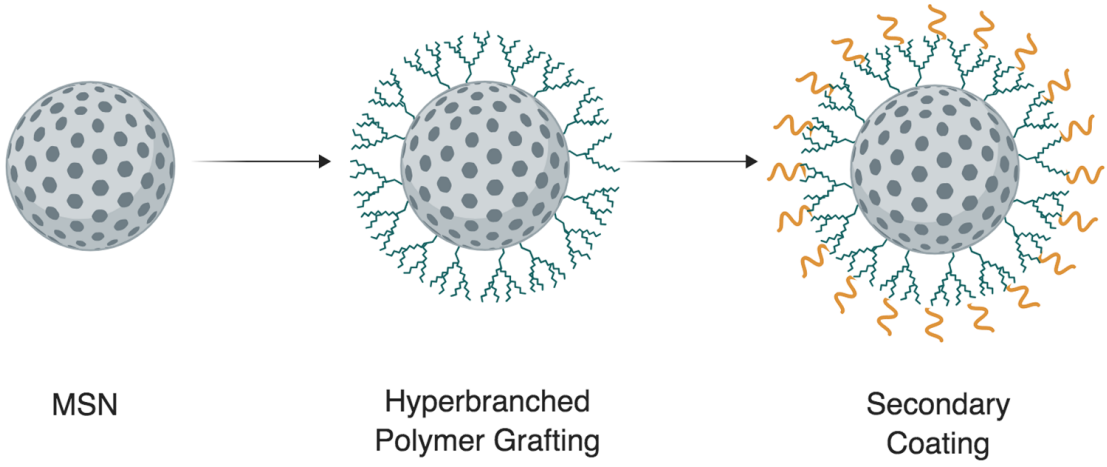

Figure 1.6.1) Schematic description of MSN surface modifications: Hyperbranched polymer (e.g. polyethylene imine (PEI)) and secondary coating (e.g. polyethylene glycol (PEG)) of mesoporous silica nanoparticles (MSNs).

1.6.2) Cellular Internalization, Cytotoxicity and Drug Delivery Efficiency of MSNs

Physiochemical properties of the nanoparticles, such as their shape, size, hydrophilicity and surface charge, significantly influence their stability and behaviour in the physiological environment (Iversen et al., 2016; Bannunah et al., 2014). Therefore, an ideal MSN surface functionalization should facilitate a high dispersion, high cellular uptake, low cytotoxicity and endosomal escape (Yue et al., 2011; Paatero, 2017).

Effect of MSN Geometry

Nanoparticle geometry is one of the parameters that affect the fate of MSNs in biological systems. Size and shape of MSNs impact their cellular internalization efficiency. For example, spherical nanoparticles are reported to show higher cellular internalization in comparison with rod-shaped nanoparticles. As for the size, the optimal interval of nanoparticle diameter to maximize cellular internalization was reported to be 20-50 nm (Chithrani et al., 2009; Jiang et al., 2008; Jin et al., 2009; Iversen et al., 2011). In addition, the size of the nanoparticles may influence the cellular pathway for their internalization. Larger particles were reported to tend to be internalized via phagocytosis, whereas smaller particles are internalized via other pathways, such as clathrin or caveolae-mediated endocytosis. On the other hand, nanoparticles with diameters larger than 500 nm were reported to be internalized predominantly via caveolae-mediated pathway; whereas those which have a diameter smaller than 200 nm were likely to be internalized via clathrin- mediated pathway (Rejman et al., 2004; Iversen et al., 2011). However, the internalization pathway greatly vary between different nanoparticle types; thus, it cannot be solely based on nanoparticle geometry.

Effect of Hydrophobicity and Surface Charge

Hydrophobicity of the nanoparticles immensely impacts their colloidal stability and intracellular fate. An ideal drug delivery tool should be sufficiently hydrophobic to interact with the membrane for membrane penetration, and hydrophilic enough for aqueous dispersion (Desai et al., 2016). Surface charge is another key factor that determines the cellular internalization, cytotoxicity as well as the distribution and residence time of MSNs in biological systems together with hydrophobicity. According to Bannunah et al. (2014); nanoparticles with high positive charge show high cytotoxicity

and cellular uptake, yet low transport efficiency (ratio of transport of the nanoparticles across the cell monolayers to cellular internalization); whereas negatively charged nanoparticles facilitate lower cytotoxicity, lower internalization, yet high transport efficiency. The surface charge of MSNs also affects the intracellular fate of the cargo molecule after the internalization. For successful cargo delivery, the nanoparticles should be able to escape endosomes and release the cargo molecules. Positively charged nanoparticles are reported to be capable of endosomal escape, whereas neutrally or negatively charged nanoparticles tend to show lysosomal co-localization (Yue et al., 2011).

1.6.3) MSN Behaviour in 3D Cell Cultures

Even though most physiochemical characteristics and cell-level behaviour of MSNs are elucidated, the current knowledge of MSNs is based on 2D *in vitro* models. However, it was demonstrated that 2D models are not sufficient to predict the nanoparticle behaviour in physiological conditions as they omit most biological parameters. The discrepancy between *in vivo* and 2D *in vitro* models by itself is a strong proof of the inadequacy of 2D models in determining the nanoparticle cytotoxicity and cellular internalization (Sayes et al., 2007). Similarly to *in vivo* cells, cells in 3D matrices, which constitute an important portion of their extracellular matrix, are highly dependent on their niche in tissue engineering scaffolds. Therefore, nanoparticle-matrix interactions cannot be overlooked by simply correlating the nanoparticle behaviour to that in 2D models, when developing a drug delivery platform to control stem cell differentiation for tissue engineering (Lee et al., 2009; Rosenholm et al., 2016).

It was reported that nanoparticle movement was hindered by 3D collagen matrices, where nanoparticles also interacted with the collagen fibres. In addition, in 3D cultures, a major portion of the cell surface are available for cellular internalization, whereas only half of the cell surface internalizes the nanoparticles in 2D models (Belli et al., 2016). Furthermore, the gene expression for the proteins responsible for the endocytosis pathways are significantly influenced by cell milieu, thus causing a difference in cellular internalization of nanoparticles between 2D and 3D models (Zschenker et al., 2012; Soares et al., 2012). Considering these factors, cytotoxicity and cellular uptake of MSNs in 3D matrices must be investigated further. However, the number of examples for such quantization of nanoparticle uptake and nanoparticle cytotoxicity in 3D cell cultures is

quite small, and the few existing studies either base the nanoparticle cytotoxicity on mean fluorescence intensity of labelled cells and nanoparticles (Belli et al., 2016; Baumann et al., 2017), or require the disruption of 3D matrix (Kessler et al., 2017). Therefore, the development of new 3D cytotoxicity/viability methodologies is a must to assess MSN behaviour in tissue engineering scaffolds.

As a conclusion, formulating printable composite bioinks, and monitoring the cellular internalization and cytotoxicity of MSNs inside 3D-printed matrices are compulsory to broaden our understanding of MSN behaviour in 3D models. This way, we can have a better control over the biological cues, and develop a systematic approach to engineer *in vitro* muscle tissue development.

2) AIMS

The major aim of this study was to formulate and 3D-bioprint an NFC based cell-laden composite hydrogel bioink for the cellular delivery of MSNs. The study includes printability optimization of composite bioink, and monitoring of the cellular viability inside the composite matrix, MSN cytotoxicity and cellular internalization of MSNs.

The milestones of the study are briefly given below:

1. Formulation and 3D-bioprinting of a NFC/GelMA composite hydrogel with high printability and post-printing fidelity and suitable stiffness, where GelMA served as an auxiliary photo-crosslinkable material.

2. Optimization of 3D-bioprining parameters for the NFC/GelMA composite hydrogel.

3. Incorporation of C2C12 mouse-derived myoblast cells inside the NFC/GelMA bioink and quantization of the cell viability, following a culture period after bioprinting and photo-crosslinking by using confocal microscopy and 3D image analysis.

4. Incorporation of MSNs with different surface functional groups (MSN-NH_2, MSN-PEI, MSN-PEI-PEG, MSN-PEI-ACA, MSN-PEI-SUCC) into the NFC/GelMA cell-laden bioink and assessment of their dispersion inside the matrix and cytotoxicity by using confocal microscopy and image analysis.

5. Selection of the MSN functional group with the least toxicity and uniform dispersity in the composite matrix, and monitoring its cellular uptake via confocal microscopy.

3) MATERIALS AND METHODS

3.1) Cell Culture and Maintenance

Mouse derived C2C12 myoblasts were used for the study. The cells were cultured in high glucose DMEM supplied with 10% FBS, 50 units/ml penicillin-streptomycin and 2 mM L-glutamine at 37°C, with 5% CO_2. The cells were maintained at a maximum cell confluency of 70% to avoid myoblast fusion and differentiation.

3.2) Preparation of the Nanoparticles

3.2.1) Sol-gel Synthesis of small TRITC-labelled MSN-NH_2

Before the nanoparticles synthesis, pro-condensation of TRITC-APTES (with a molar ratio of 1:3 was performed inside ethanol. 150 ml of H_2O, 30 ml of ethylene glycol and 450 mg CTAB was mixed and heated to 70°C inside a 3-neck glass bottle under constant stirring. 2.1 ml of decane was added to the solution and let homogenize for 30 minutes. 0.51 ml of TMB was added as a swelling agent into the reaction media and let mix for 90 minutes. 2.5 ml ammonium hydroxide (32% wt), 0.3 ml APTES and 1.5 ml TEOS were added into the reaction media respectively. The reaction media was stirred for 3 hours. Afterwards, the stirrer was discarded and the reaction media was let be overnight. The molar ratio for the reaction was 0.19 APTES : 1TEOS : 0.36CTAB : 3.2decane : 1.1TMB : 5.9NH_3 : 88.5ethylene glycol : 1249H_2O. The particles were then calcinated with an extracted solution containing 1.17 M ammonium nitrate in ethanol. The resulting particles were kept in ethanol. Transparent MSNs were synthesized according to the same protocol without TRITC labelling.

3.2.2) Surface Functionalization

Polyethylene imine (PEI) Functionalization on TRTIC-MSN-NH_2

In order to functionalize MSN-NH_2 with PEI, 200 mg of TRITC-MSN-NH_2 particles was first re-dispersed in 20 ml of toluene. Under constant stirring the suspension was heated

to 50°C. Then 10.4 µl of acetic acid and 104 µl of aziridine was added into the reaction media respectively. The reaction media was let reach 70°C and stirred overnight. The next day, the particles were washed with ethanol, and stored in ethanol.

Polyethylene Glycol (PEG) Functionalization on TRITC-MSN-PEI

For PEG functionalization of TRITC-MSN-PEI, 40 mg of activated mPEG (5000 kDa) was dissolved in 10 ml of chloroform, where 20 mg of TRITC-MSN-PEI was dispersed in a separate 10 ml volume of chloroform. MSN-PEI stock was then mixed with the mPEG solution inside a glass balloon and heated to 60°C under constant stirring, while connected to a condensation unit. The reaction media was stirred overnight. The next day, the particles were washed with ethanol and stored in ethanol.

Acetic Anhydride (ACA) Functionalization on TRITC-MSN-PEI

ACA functionalization was started by dissolving 185.1 µL of acetic anhydride (d=1.08 g/mL) in 20 mg of ethanol. 20 mg of TRITC-MSN-PEI was added into the reaction media and stirred overnight at 400 RPM overnight. The next day, the particles were washed with ethanol and stored in ethanol.

Succinic Anhydride (SUCC) Functionalization on TRITC-MSN-PEI

SUCC functionalization was started by dissolving 200 mg of succinic anhydride in 20 mg of ethanol. 20 mg of TRITC-MSN-PEI was added into the reaction media and stirred overnight at 400 RPM overnight. The next day, the particles were washed with ethanol and stored in ethanol.

3.2.3) Characterization of MSNs

Hydraulic diameter and ζ-potential measurements were performed by using Zetasizer to quality-check the nanoparticles. Two separate samples of nanoparticle suspension with a concentration of 100 µg/mL were prepared in ethanol and 1X HEPES (25 mM, pH 7.4) for hydraulic diameter and ζ-potential measurements, respectively. In addition, the size of the MSNs was verified by using transmission electron microscopy (TEM).

3.2.4) DiD loading into Functionalized MSNs

1,1'-Dioctadecyl-3,3,3',3'-Tetramethylindodicarbocyanine (DiD) fluorophore was used as a model drug for assessment of the intracellular drug delivery capability of the MSNs. To load the nanoparticles with 5% (w/w) DiD (Invitrogen), 10 mg TRITC-MSN-PEI in ethanol stock was centrifuged at 13 500 RPM for 15 minutes, the supernatant was discarded. The pellet was re-dispersed in 5 mL of cyclohexane solution, where 0.5 mg of DiD was dissolved in another 10 ml volume of the same solvent. The tubes were then sonicated using Covaris focused ultra-sonicator. The dye solution was then added into the nanoparticle suspension under constant sonication. The tube was then sealed and rotated at 60 RPM overnight for loading. The next day, the nanoparticles were collected and vacuum-dried overnight. The same protocol was repeated for TRITC-MSN-PEI-PEG, TRITC-MSN-PEI-ACA and TRITC-MSN-PEI-SUCC.

3.3) Preparation of NFC/GelMA Composite Bioink

TEMPO-oxidised NFC (1% w/v) was synthesized by Ezgi Özliseli at Åbo Akademi Laboratory for Wood and Paper Chemistry. In order to prepare 1 ml of NFC/GelMA composite bioink with 0.9% (w/v) NFC and 4.5% (w/v) GelMA (Advanced Biomatrix) concentration, 900 µL of NFC was taken into a sterile 2 ml centrifuge tube. 15 µg phenol red, 4.5 of mg powdered DMEM, 0.5 µL of 1M KOH and 100 µL of 10X HEPES buffer (250 mM, pH 7.4) were mixed into NFC respectively by using a syringe and a vortex mixer. 2.5 mg of Irgacure 2959 was then dissolved in 100 µl of milliQ water at 70°C inside a water bath. The Irgacure 2959 solution was then mixed into the NFC mixture. Afterwards, 50 mg of GelMA was weighed and taken into a separate sterile 2 ml centrifuge tube. The NFC mixture was added on top of GelMA and centrifuged at 1000 RPM for 60 seconds. The mixture was then kept at 37°C in a water bath for 2 hours and mixed by using a vortex mixer every 30 minutes.

3.3.1) Preparation of NFC/GelMA Composite Bioink with small TRITC-MSN

In order to disperse TRITC-MSN-PEI inside NFC, 15 µl of TRITC-MSN-PEI suspension with 10 mg/ml (in DMSO) concentration was re-dispersed in 100 µL of 10X HEPES buffer (250 mM, pH 7.4) inside a 2 ml centrifuge tube by sonicating. The NFC mixture

was then gradually mixed into the TRITC-MSN suspension. The TRITC-MSN/HEPES mixture was sonicated and vortexed after each NFC addition. Then, 1 ml of NFC/GelMA composite bioink with 0.9% (w/v) NFC and 4.5% (w/v) GelMA and 150 µg/mL MSN concentration, was prepared according to the protocol given in **Section 3.3**. The same protocol was repeated for TRITC-MSN-PEI-PEG, TRITC-MSN-PEI-ACA and TRITC-MSN-PEI-SUCC.

3.3.2) Preparation of NFC/GelMA Composite Cell-laden Bioink with small MSN

The initial cell number for the bioink preparation was estimated to be 10^7 cell/ml (Laternser et al., 2018). 5 µl of MSN suspension with 10 mg/ml (in EtOH) was re-dispersed in NFC as described in **Section 3.3.1**. 10^7 cells were counted and spun down into a 2 mL centrifuge tube. The cell pellet was re-dispersed in the NFC mixture before the addition of GelMA. Then, 1 ml of NFC/GelMA composite cell-laden bioink with 0.9% (w/v) NFC and 4.5% (w/v) GelMA and 50 µg/mL MSN concentration was prepared as described in **Section 3.3** by re-dispersing cell pellet in the NFC mixture, before adding GelMA. The same protocol was repeated for MSN-PEI, MSN-PEI-PEG, MSN-PEI-ACA, MSN-PEI-SUCC and the control. The corresponding volume of ethanol was separately added into the control.

3.3.3) Preparation of NFC/GelMA Composite Cell-laden Bioink with DiD Loaded TRITC-MSN-PEI-SUCC

To disperse the DiD-loaded TRITC-MSN-PEI-SUC powder inside NFC, 500 µl of stock with a TRITC-MSN-PEI-SUCC concentration of 1mg/mL was prepared by adding 500 µg nanoparticle powder into 500 µl 10X HEPES buffer (250 mM, pH 7.4). The suspension was then sonicated for 30 minutes, and vortexed every 10 minutes. To achieve a better dispersion, the suspension was sonicated with focused-ultrasonicator (Covaris) for 3 minutes. 100 µL of TRITC-MSN-PEI-SUC stock with 500 µg/mL TRITC-MSN-PEI-SUCC concentration (in 10X HEPES buffer 250 mM, pH 7.4) was prepared, and sonicated for 10 minutes for nanoparticle dispersion. The stock was then re-dispersed in the NFC mixture as described in **Section 3.3.1.** NFC/GelMA composite cell-laden bioink with DiD loaded TRITC-MSN-PEI-SUCC was then prepared as described in **Section 3.3** and **Section 3.3.2**.

3.4) 3D-Bioprinting

3.4.1) Computer-Aided Design of the 3D Model

A dumbbell-shaped object (Laternser et al., 2018) with a size of 16.0x3.0x1.6 mm (length x width x height) was designed using Google Sketchup Make 2016, and the resulting object was exported as a ".stl" file. The design file was then converted to a G-code file using Repetier Host and embedded Slic3r software. A concentric printing pattern that mimics the linear structure of native skeletal muscle bundles was achieved by setting the infill density to 0% and increasing the number of perimeters until the entire volume of the object was filled (**Figure 3.4.1**).

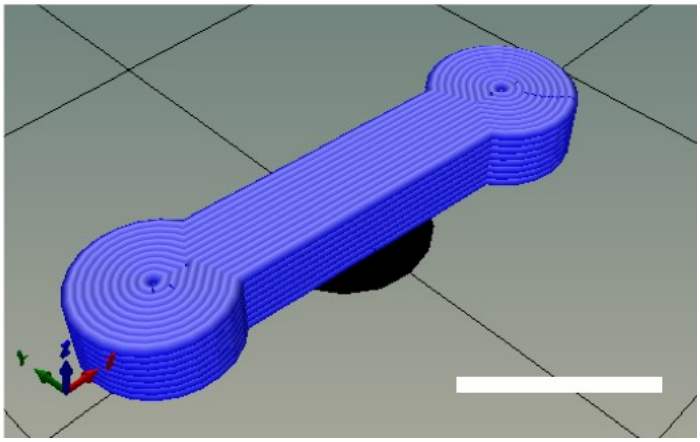

Figure 3.4.1) Visualization of the printing configuration for the NFC/GelMA composite bioink: Visualization of the G-code of the dumbbell-shaped model prepared for the 3D-printing of the NFC/GelMA composite bioink (Scale bar: 6 mm).

3.4.2) 3D-Bioprinting of the NFC/GelMA composite Bioink

A sterile 10 ml syringe (BD Life Sciences) was used as a bioink vessel. The rubber tip of the syringe plunger was removed by using a pair of forceps. The top piece of the plunger was cut off by using a pair of scissors in order to prevent rubber tip to attach to the plunger. The NFC/GelMA composite bioink was then loaded into the syringe. The rubber tip was pushed into the syringe by using the plunger until the bioink reached to the tip of the syringe. A printing needle (25G and 30G) was then attached to the syringe. Afterwards, the syringe was connected to the bioprinter. For the 3D-printing process,

Allevi 2 (Biobots) (**Figure 4.5.2**) extruder-based bioprinter was used. A 35 mm glass bottom dish with a microwell diameter of 20 mm was placed and secured on the printing plane to serve as both a printing vessel and a culture plate, and the device was calibrated. The G-code corresponding to the CAD model was uploaded to the server, and printing was performed. After the printing, the resulting structure was irradiated with UV (365 nm) for crosslinking, and let sit for 10 minutes. Culture media was added on printed scaffolds until covered, and scaffolds were incubated at 37°C with 5% CO_2.

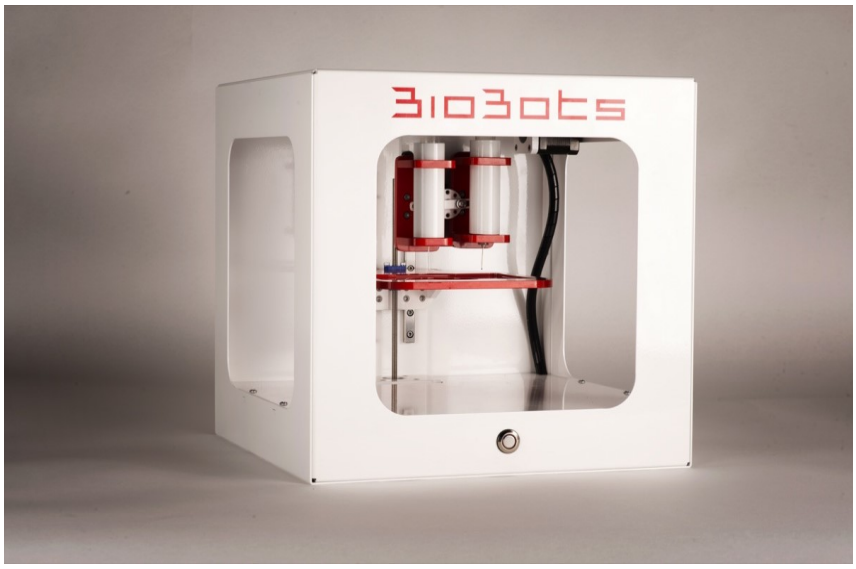

Figure 4.5.2) The EBB printer used for the study: Allevi 2 (Biobots) Extruder Based Bioprinter (EBB) that is used for the 3D-bioprinting of the NFC/GelMA composite bioink.

3.4.3) Optimization of GelMA concentration for 3D-printing

NFC/GelMA composite hydrogels with a GelMA concentration of 0.1% (w/v), 0.9% (w/v), 4.5% (w/v) and 9.9% (w/v) was prepared and 3D-printed for the tuning of the bioink's printability. The results were qualitatively compared to the printability of the pure NFC (1% w/v).

3.4.4) Optimization of 3D-printing parameters for the NFC/GelMA Composite Bioink

Three different layer height values were tested for each of 30G and 25G needles to optimize the printing resolution. The printing configurations that are used for the optimization of the 3D-printing of the NFC/GelMA composite bioink are given in **Table 3.4.4.a** and **3.4.4.b**.

Table 3.4.4.a) Printing configuration used for the 3D-printing of the NFC/GelMA composite bioink.

Speed	
Print Moves (mm/s)	2
Perimeters (mm/s)	2
Small Perimeters (mm/s)	2
External Perimeters (mm/s)	2
Travel Speed (mm/s)	4
First Layer Speed (mm/s)	2
Max Print Speed (mm/s)	2
Max Volumetric Speed (mm/s)	2
Extruders	
Perimeter Extruder	2
Temperature (∘C)	24
Other Settings	
Infill Density (%)	0
Fill Angle (∘)	45
Solid Infill Threshold Area (mm2)	70

Table 3.4.4.b) Settings tested for the optimization of the 3D-Printing resolution of NFC/GelMA composite bioink with 30G and 25G needles.

Needle Gauge	Resolution Settings			
30G	Layer Height (mm)	0.16	0.20	0.25
	First Layer Height (mm)	0.16	0.20	0.25
	Number of Perimeters	19	15	12
	Pressure Interval (psi)	15-28		
25G	Layer Height (mm)	0.26	0.33	0.4
	First Layer Height (mm)	0.26	0.33	0.4
	Number of Perimeters	12	9	7
	Pressure Interval (psi)	6-18		

3.4.5) UV Photo-crosslinking and Crosslinking Optimization

A cell-laden NFC/GelMA bioink was prepared as described in **Section 3.3.2**. The resulting structure was exposed to a UV source (365 nm) for 30, 60 and 120 seconds to optimize the photo-crosslinking density of GelMA inside the NFC matrix. The structures were then let sit for 10 minutes, and incubated in cell media for 7 days at 37°C, 5% CO_2. The results were photographed to evaluate the decomposition of the matrix inside the cell media.

3.4.6) Estimation of Mechanical Properties

For the mechanical measurements, an NFC/GelMA composite disc with a size of 3x4 mm (diameter x height) was printed and UV photo-crosslinked for 60 seconds. The compressive properties of the photo-crosslinked NFC/GelMA composite was measured by using a commercial TA.XTplusC texture analyser and Exponent software with a 5 mm diameter probe, a constant compression speed of 0.1 mm/s, and a trigger force of 5 N. The elastic modulus of the composite matrix calculated based on the slope of the elastic region of the stress/strain curve.

3.5) Nanoparticle Distribution inside the NFC/GelMA Composite Matrix

NFC/GelMA composite bioinks with TRITC-MSN-PEI, TRITC-MSN-PEI-PEG, TRITC-MSN-PEI-ACA and TRITC-MSN-PEI-SUCC with a nanoparticle concentration of 150 µg/ml were prepared as described in **Section 3.3.1**. The bioinks were then 3D-printed and UV photo-crosslinked for 60 seconds. The resulting structures were let sit for 10 minutes, and incubated in 1X HEPES buffer (25 mM, pH 7.4) at room temperature. The samples were imaged as Z-stacks with a slice thickness of 5 µm and a total thickness of 200 µm, with Plan-Apochromat 20X/0.8 objective by using LSM 780 confocal microscope (Zeiss). TRITC was excited with 543 nm HeNe laser, and its emission was collected at 551-637 nm. The resulting images were then rendered by using Zeiss LSM Blue software.

3.6) C2C12 Cell Viability and MSN Cytotoxicity inside the NFC/GelMA Composite Matrix

A cell-laden NFC/GelMA composite bioink with a cell concentration of 10^7 cell/ml and an MSN concentration of 50 µg/ml was prepared as described in **Section 3.3.2**. The bioink was then 3D-printed and UV photo-crosslinked for 60 seconds. The same protocol was repeated for MSN-PEI, MSN-PEI-PEG, MSN-PEI-ACA and MSN-PEI-SUCC. The resulting structures were let sit for 10 minutes and then incubated in cell media at 37°C, with 5% CO_2 for 7 days.

3.6.1) Live/Dead Staining and Confocal Microscopy

The live/dead staining solution with 2 µM calcein AM and 7.5 µM propidium iodide concentrations (Thermo Fisher) was prepared by mixing the stock solutions in 1X PBS buffer (pH 7.4) and sonicating. After discarding the cell media, the samples were stained by incubating the structures in 1 ml of the staining solution for 45 minutes at room temperature. The stained samples were imaged as Z-stacks with a slice thickness of 5 µm and a total thickness of 200 µm with EC Plan-Neofluar 10x/0.3 objective by using LSM 780 confocal microscope (Zeiss) on day 1 and day 7 after implementation. Calcein AM was excited with 488 nm Argon laser, and the emission was collected at 490-530 nm. Propidium iodide was excited with 514 nm Argon laser, and its emission was collected at 600-670 nm. Three Z-stack images were taken per sample for statistical analysis of the cell number.

3.6.2) 3D Image Analysis and Cell Count

Fiji ImageJ was used to analyse the Z-stack images in order to calculate the number of the live and dead cells inside the hydrogel matrix. First, multichannel images were split into channels where the green and red channels correspond to live and dead cells, respectively. Each sample was processed with histogram equalization for signal amplification, and Gaussian filter with a sigma value of 2.00 for noise-cancelling. The number of the objects in each channel was then counted by using 3D Object Count Plug-in (**Figure 3.6.2**). The data acquired was then statistically analysed with student's t test to estimate the %viability in each sample with respect to the control.

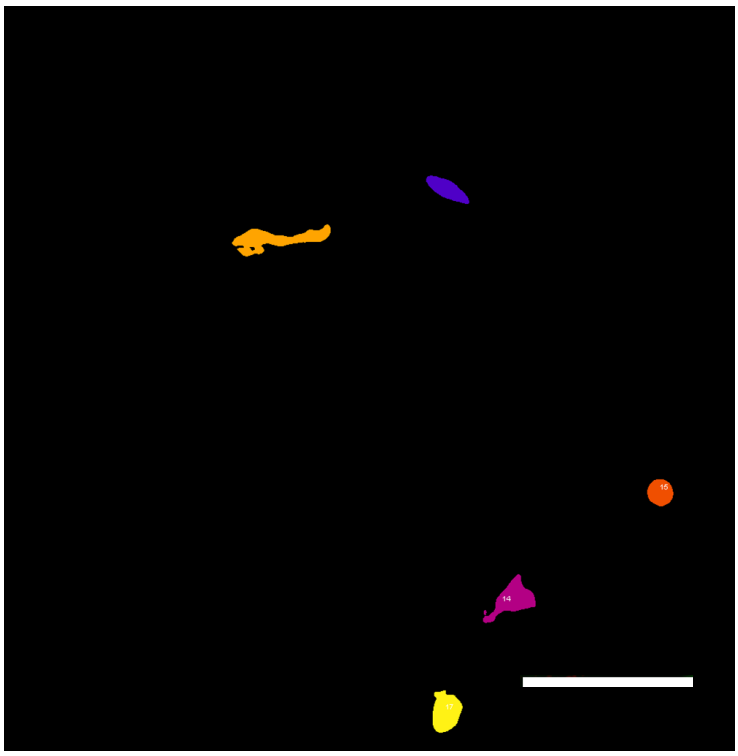

Figure 3.6.2) 3D Object Count in the NFC/GelMA composite matrix: Segmentation and counting of the cells in the green channel of a Z-stack image of the cell-laden NFC/GelMA composite matrix by using Fiji ImageJ. (Separate objects are represented with different colours, scale bar: 100 µm)

3.7) Cellular Uptake of TRITC-MSN-PEI-SUCC loaded with DiD inside NFC/GelMA Composite Matrix

A cell-laden NFC/GelMA composite bioink with a cell concentration of 10^7 cells/ml and a TRITC-MSN-PEI-SUCC/DiD concentration of 50 µg/ml and was prepared as described in **Section 3.2.3**. The bioink was then 3D-printed and UV photo-crosslinked for 60 seconds. The resulting structures were let sit for 10 minutes and then incubated in cell media at 37°C with 5% CO_2 for 7 days.

3.7.1) Cytoplasm Staining and Confocal Microscopy

The staining solution with 2 µM calcein AM concentration was prepared by mixing the stock solution in 1X PBS buffer (pH 7.4) and sonicating. After discarding the cell media, the samples were stained by incubating the structures in 1ml of the staining solution for 45 minutes at room temperature. The stained samples were imaged as Z-stacks with a

slice thickness of 0.5 µm with Plan-Apochromat 100X/1.40 Oil DIC objective by using LSM 780 confocal microscope (Zeiss) on day 1, 3 and 7. Calcein AM, TRITC and DiD were excited with 488, 543 and 633 nm lasers, and their emission was collected at 493-616, 551-637 and 638-756 nm spectra, respectively.

3.7.2) 3D-Rendering of the Z-Stack Images

Z-stack images were rendered in 3D by using Imaris software (Oxford Instruments) for better a visualization of the cellular internalization of the nanoparticles. For the image rendering, the histogram was equalized for each of the channels, where the red, green and blue channels correspond to TRITC, calcein AM and DiD respectively. The image data were thresholded to segment the image for each channel. The objects were then represented as surfaces.

4) RESULTS

4.1) TRITC-MSN Synthesis Met the Quality Criteria

The TRITC-MSN-NH_2 was collected into EtOH (Aa grade 99.5% v/v), and its dynamic size and ζ-potential were assessed in EtOH and 1X HEPES buffer (25 mM, pH 7.4) via dynamic light scattering (DLS) and zeta (ζ) potential measurements, respectively. The dynamic size of the freshly synthesized nanoparticles was found to be 181.0±3.6 nm (Polydispersity index (PDI): 0.071±0.050), whereas its zeta potential was 5.84±1.05 mV. The reliability of the measurement was supported by raw correlation data and the normal distribution of the size (**Figure 4.1.2**). TEM imaging also showed that nanoparticle diameter was approximately 50 nm (**Figure 4.1.3**). Upon the successful synthesis, 200 mg of the nanoparticles were prepared for PEI functionalization. After the PEI functionalization, the dynamic size and the zeta potential of the nanoparticles changed to 188.4±1.9 nm (PDI: 0.098±0.016) and 32.6±1.35 mV, respectively. MSN-PEI was then functionalized with PEG, ACA and SUCC. Their hydrodynamic sizes and zeta potentials of the particles are given in **Table 4.1.1**. Based on the DLS measurements, the properties of the MSNs complied with the previous studies (Paatero et al., 2017) and the surface functionalization procedures were agreed to meet the quality criteria. The MSNs were then loaded with 5% DiD.

Table 4.1.1)**The size and the surface charge of the MSNs:** Dynamic size and zeta (ζ) potential of the TRITC-MSNs with different surface functional groups measured by using using dynamic light scattering (DLS).

	d (nm)	PDI	ζ (mV)
TRITC-MSN-NH_2	181.0±3.6	0.071±0.050	+6.8±0.2
TRITC-MSN-PEI	188.4±1.9	0.098±0.016	+32.6±1.4
TRITC-MSN-PEI-PEG	198.9±1.5	0.126±0.071	+11.0±1.1
TRITC-MSN-PEI-ACA	184.0±0.1	0.012±0,083	-10.0±0.3
TRITC-MSN-PEI-SUCC	186.4±4.5	0.111±0.057	-42.6±0.1

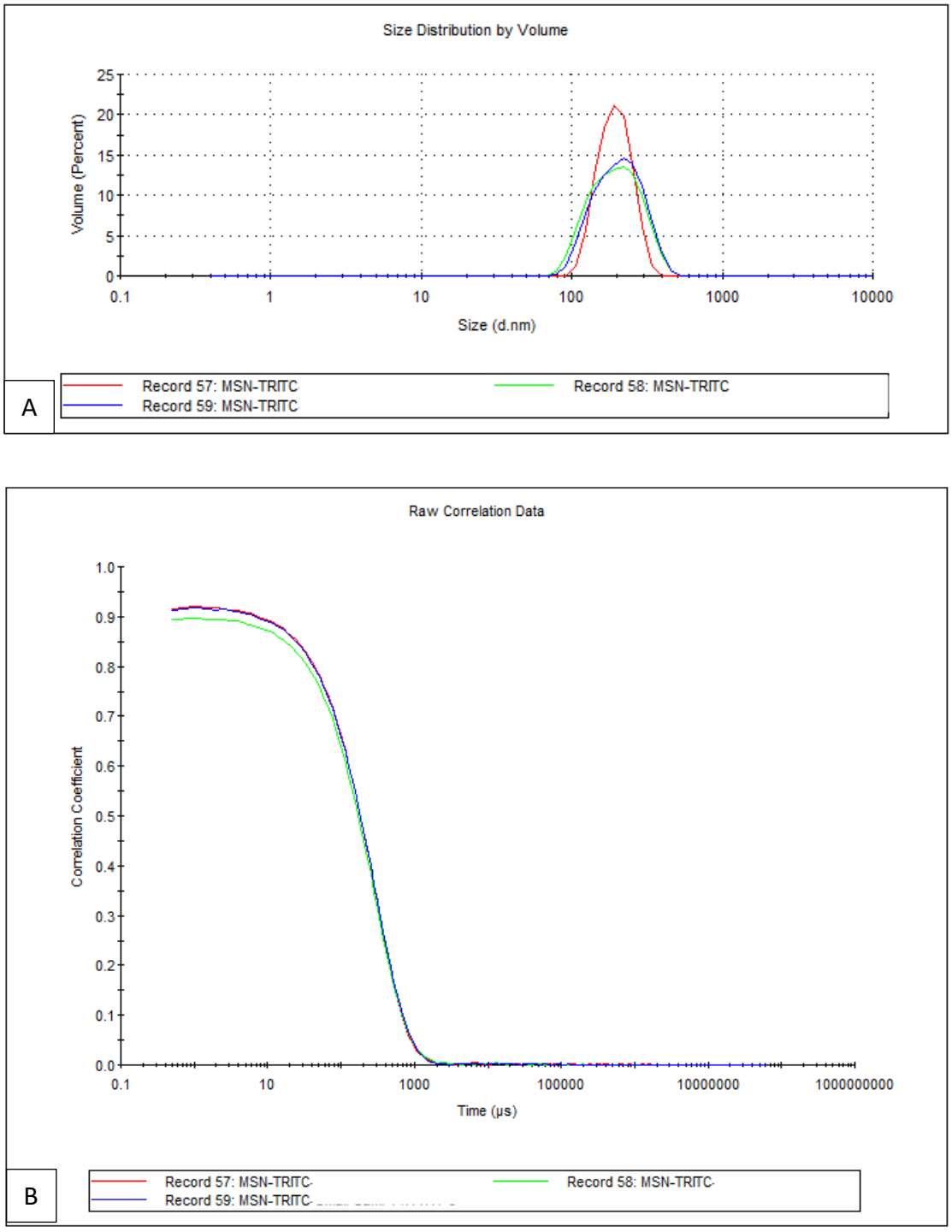

Figure 4.1.2) The DLS measurement of the MSNs is reliable: The size distribution (A) and the raw correlation data (B) of TRITC-MSN-NH_2 received from the dynamic light scattering (DLS) measurement meets the quality criteria and supports the reliability of the measurement.

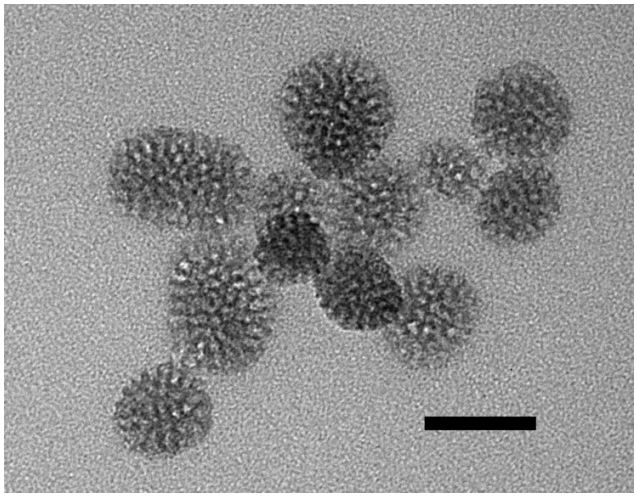

Figure 4.1.3: **TEM image of the MSNs:** Transmission electron microscopy (TEM) image of the small MSN particles show that the MSNs are approximately 50 nm in

4.2) Cell-laden NFC/GelMA Composite Bioink Showed Excellent Printability and Post-Printing Fidelity

Three different NFC/GelMA bioinks with GelMA concentrations of 0.9% w/v, 4.5% w/v and 9.9% w/v; and pure NFC (1%) were 3D-printed. Pure NFC (1% w/v) showed poor printability due to its low concentration, and spread already after the printing of the first layer. NFC/GelMA (0.9% w/v, 0.9% w/v) underwent phase separation, where only liquid drops were dispensed from the needle; thus, it could not be printed. NFC GelMA (0.9% and The NFC/GelMA bioink with high GelMA concentration (0.9% w/v, 9.9% w/v) was able to be dispensed as fibres, yet it caused clogging of the needle.

Among the four formulations, NFC/GelMA (0.9% w/v, 4.5% w/v) composite bioink showed an excellent printability. Even without photo-crosslinking, each bioink layer stayed firm on top of the previous layer, and maintained clear boundaries during the printing, suggesting that the bioink has high fidelity. With the high cell concentration (10^7 cells/ml), incorporation of the cells and MSNs did not significantly affect the printability properties of the bioink. Furthermore, both 25G and 30G needles facilitated high resolution and precise printing. However, due to the long printing time and higher pressure required for 30G needle, 25G needle was used for the rest of the study. For the 25G needle, the optimal printing resolution was achieved at a pressure interval of 8-12 psi and 0.4 mm layer thickness with a constant printing speed of 2 mm/s, which resulted

in a good match between the theoretical and actual layer thickness values (**Figure 4.2**). On the other hand, different pressure and layer thickness values resulted in excessive bubble formation or poor resolution.

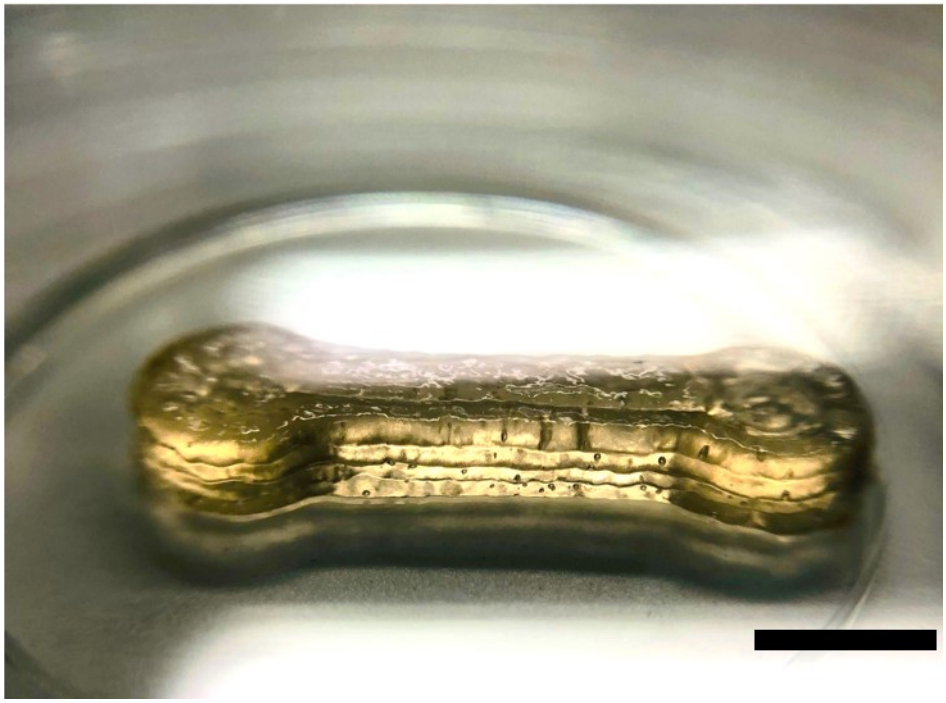

Figure 4.2) The printability of the NFC/GelMA composite bioink: The cell-laden NFC/GelMA (0.9% w/v, 4.5% w/v) composite structure after printed with 25G needle (10^7 cell/ml pressure: 8-12 psi, layer thickness: 0.4 mm, scale bar: 6 mm).

4.3) The Effect of UV Irradiation on GelMA Crosslinking and Morphological Integrity of the NFC/GelMA Composite Matrix in Cell Media

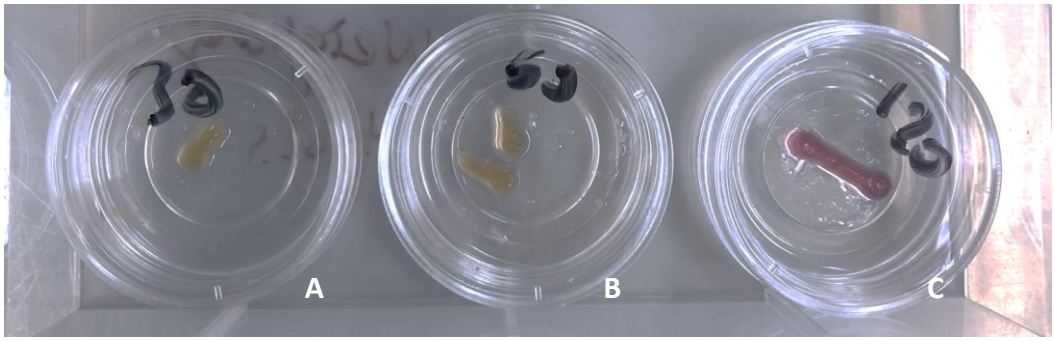

Figure 4.3.a) Crosslinking density affects NFC/GelMA integrity in cell media: UV photo-crosslinked cell-laden NFC/GelMA (0.9% w/v, 4.5% w/v) composite structures that were irradiated with UV (365 nm), after 7 days of incubation inside cell media at 37°C with 5% CO_2 (UV irradiation times: A: 30 seconds, B: 60 seconds, C: 120 seconds).

The effect of UV (365 nm) irradiation for 30, 60 and 120 seconds on GelMA crosslinking in NFC was investigated by storing the cell-laden NFC/GelMA (0.9% w/v, 4.5% w/v) composite structure inside cell media at 37°C, 5% CO_2 for 7 days after the printing (**Figure 4.3.a**). Among the three groups, the bioink irradiated with UV for 120 seconds showed the highest morphological integrity. However, when irradiated with UV for 60 seconds, the bioink maintained enough of integrity. Therefore, 60 seconds of UV irradiation was used for the rest of the study, considering UV irradiation can be toxic to the cells.

Furthermore, the morphological integrity of NFC/GelMA inside cell media was affected not only by UV irradiation, but also the thickness of the printed structure. When the dumbbell shaped structure was printed with a thickness of 0.8 mm instead of 1.6 mm for the live/dead assay, due to the limitations to the propylene iodide penetration (**Figure 4.3.b** and **4.3.c**), the structure partially decomposed inside the cell media after 7 days, and fully decomposed after 14 days, despite the same UV irradiation time.

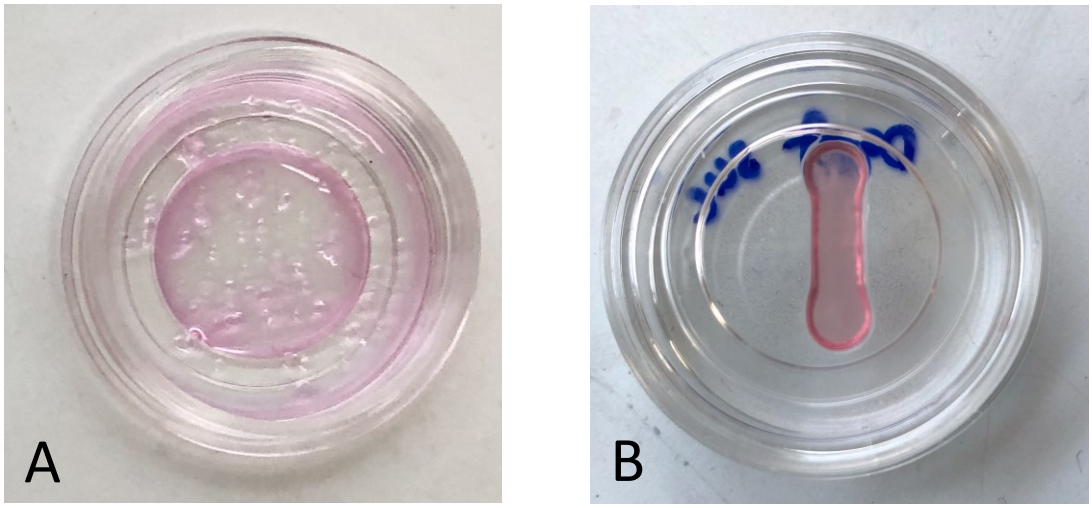

Figure 4.3.b) NFC/GelMA integrity in cell media is affected by thickness: The cell-laden NFC/GelMA (0.9% w/v, 4.5% w/v) composite matrices with two different thicknesses (A:0.8 mm, B: 1.6 mm), after irradiated with UV for 60 seconds and incubated in cell media for 14 days.

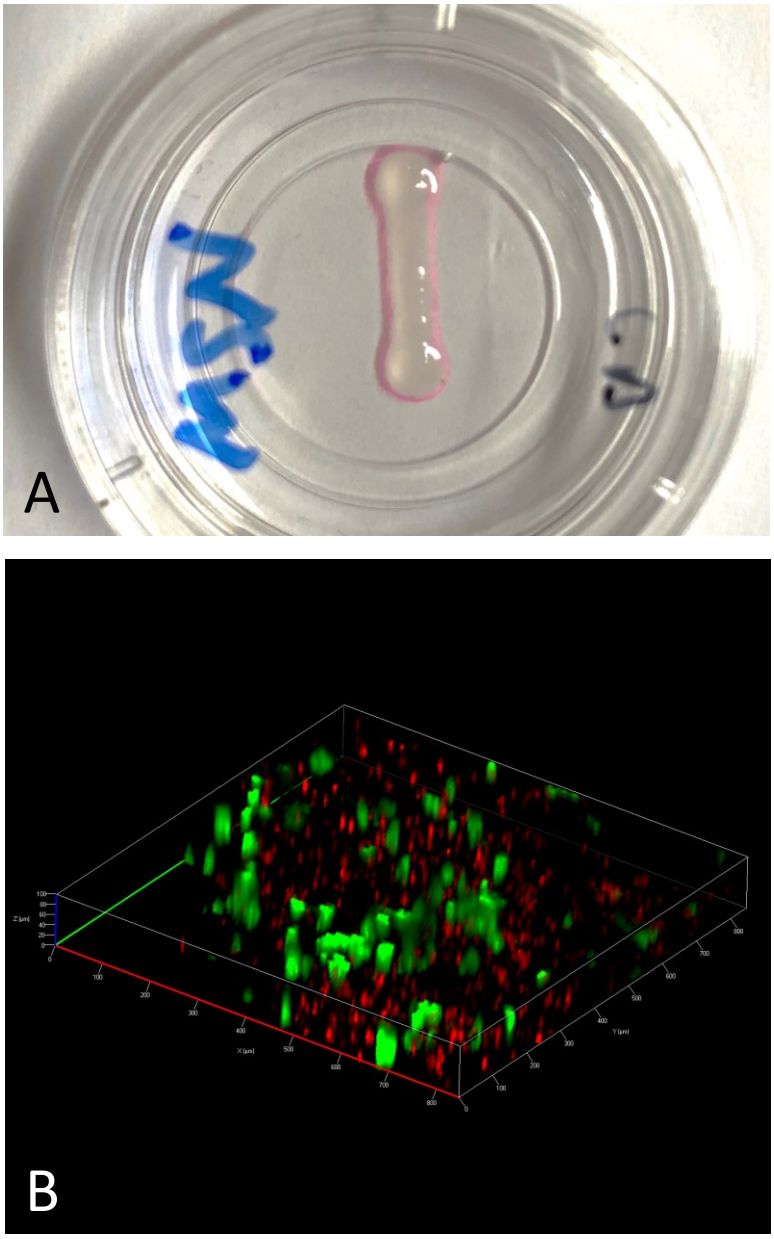

Figure 4.3.c) The thickness of the NFC/GelMA matrix affects the live/dead staining dye penetrance: Propylene iodide (red) could not penetrate the cell-laden NFC/GelMA (0.9% w/v, 4.5% w/v) matrix with 1.6 mm after UV irradiation of 60 seconds, and stained only the nuclei on the walls of the printed structure (A: macro photograph of sample, B: z-stack image acquired with confocal microscopy after live/dead staining (green:live, red:dead) , z-stack size: 0.84x0.84x0.1 mm (XxYxZ axes)).

4.4) NFC/GelMA (0.9% w/v, 4.5% w/v) Showed High Stiffness When Photo-Crosslinked for 60 seconds

In order to estimate the stiffness value of the NFC/GelMA composite bioink after 60 seconds of UV irradiation, a compression test was applied. The stress/strain curve of the crosslinked matrix is given in **Figure 4.4**. To measure the stiffness of the composite matrix, the elastic modulus was calculated to be 75.1 kPa, based on the slope of the elastic region of the stress/strain curve.

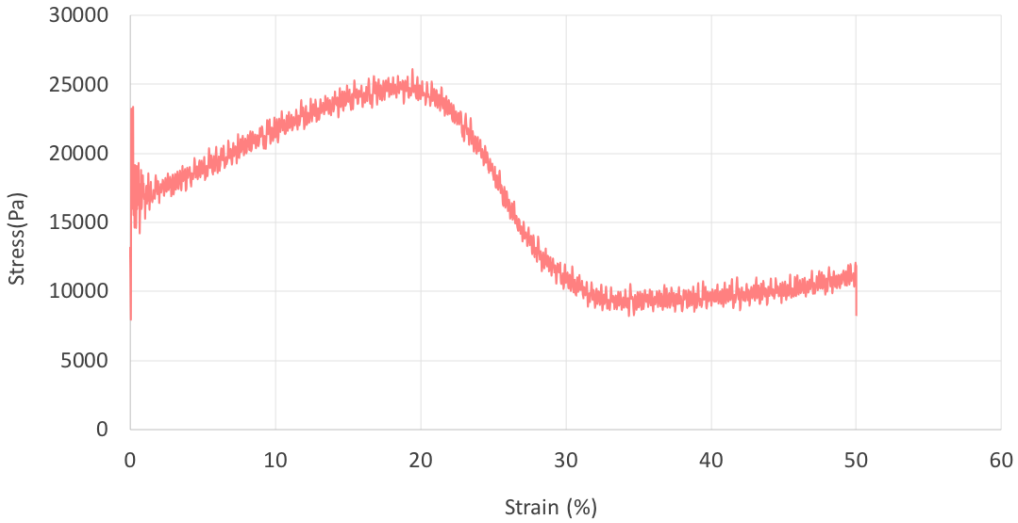

Figure 4.4) Stiffness Measurement of the NFC/GelMA (0.9% w/v, 4.5% w/v) Composite Matrix: Stress (Pa)/Strain (%)curve of the NFC/GelMA (0.9% w/v, 4.5% w/v) matrix (3x4 mm, diameter x height) after 60 seconds of UV irradiation (365 nm), based on the compression data.

4.5) Viability of C2C12 Cells Incorporation in NFC/GelMA Composite Matrix was lower than 20%

In order to estimate cell viability inside NFC/GelMA composite matrix by using confocal microscopy, the cells were stained with live/dead staining. After the staining, the green fluorescence was emitted from the live cell cytoplasm, whereas the red fluorescence was emitted from the nuclei of the dead cells. The images of the scaffold sections and the cell viability quantization data acquired by using Fiji ImageJ on day 1 and day 7 after the printing are given in **Figure 4.5.a** and **Figure 4.5.b**, respectively. 24 hours after the printing the cellular viability inside the composite matrix was calculated to be

18.04±1.29% (mean±SEM). On the seventh day following the printing, the viability was as low as 14.48±1.84%. Furthermore, even on day 7, cellular attachment in NFC/GelMA composite matrix was poor. Based on the microscopy images, the cells were uniformly distributed inside the matrix.

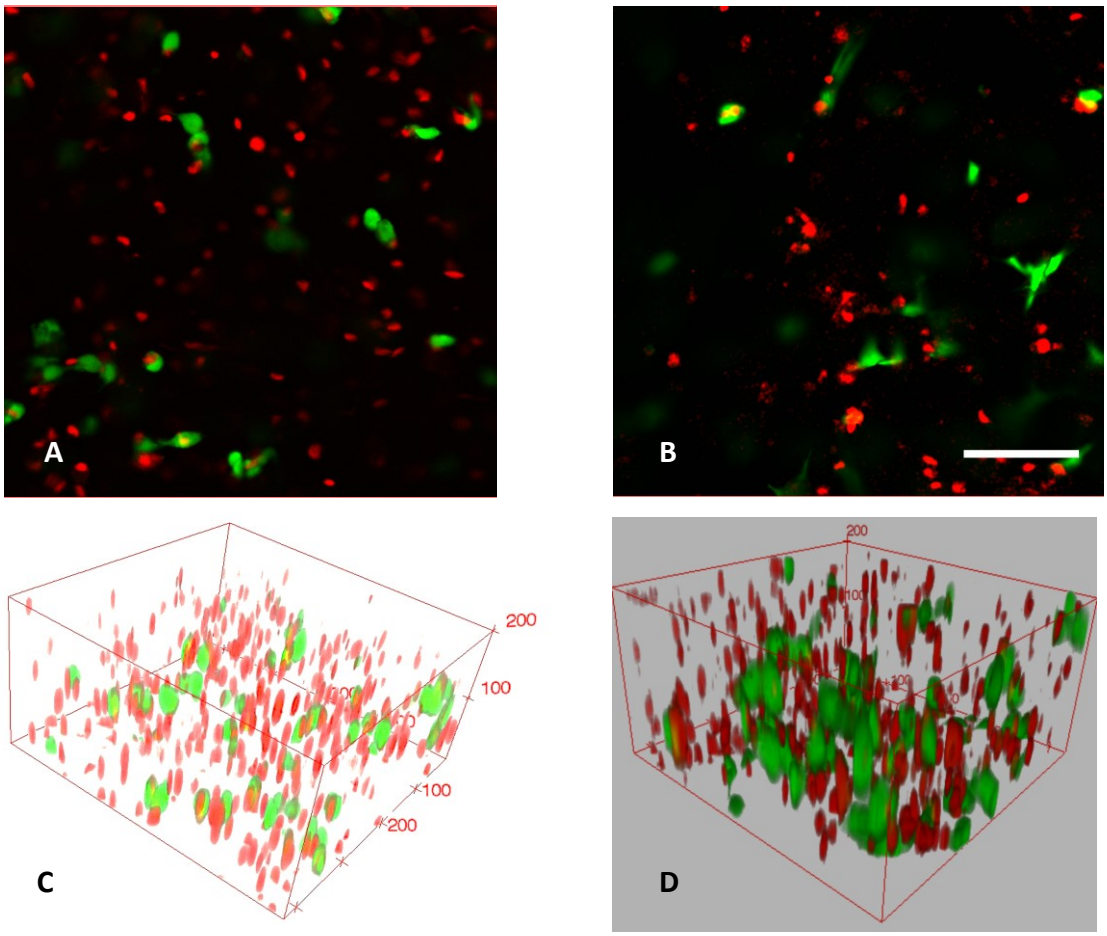

Figure 4.5.a) Live/Dead Images of the C2C12 cells in the NFC/GelMA composite matrix: Confocal microscopy images of C2C12 cells incorporated in the NFC/GelMA (0.9 w/v, 4.5 w/v) composite bioink UV photo-crosslinked and stained with live/dead staining (green: live, red: dead) [A,B: 2D slices from the Z-Stack confocal images; C,D: 3D rendering of the z-stack images (0.42x0.42x0.2 mm, XxYxZ axes) on day 1 and day 7 respectively, scale bar: 100 µm].

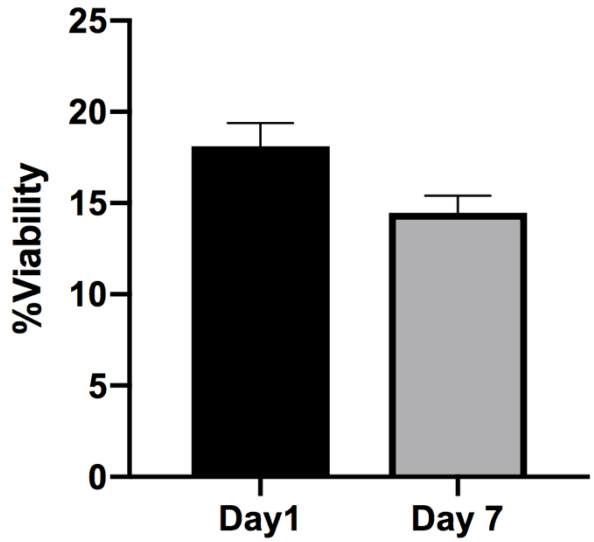

Figure 4.5.b) Viability inside the NFC/GelMA composite matrix declined over time: Based on the image analysis of the live/dead assay, %viability of C2C12 cells inside the photo-crosslinked NFC/GelMA (0.9 w/v, 4.5 w/v) matrix on day 1 and day 7 were 18.04±1.29% and 14.48±1.84%, respectively. Bar=mean±SEM, n=3.

4.6) Nanoparticle Cytotoxicity inside Photo-crosslinked NFC/GelMA composite Matrix

The cytotoxicity of MSNs with 50µg/mL concentration to the cells encapsulated in NFC/GelMA (0.9 w/v, 4.5 w/v) composite matrix was tested with live/dead staining and consequent object count in the Z-stack images on day 1 and day 7. The results were statistically analysed, and expressed as viability% relative to the viability of the control on day 1. The incorporation of MSNs in hydrogel composite caused lower viability in a time-dependent manner (**Figure 4.6**). On day 1, MSN-PEI and MSN-PEI-PEG showed similar cell viability to that of the control, whereas the lowest viability was showed by MSN-PEI-SUCC. However, the viability in the sample with MSN-PEI dramatically dropped over time, and showed the lowest viability; whereas MSN-PEI-SUCC, MSN-NH_2, MSN-PEI-PEG and MSN-PEI-ACA showed similar viability.

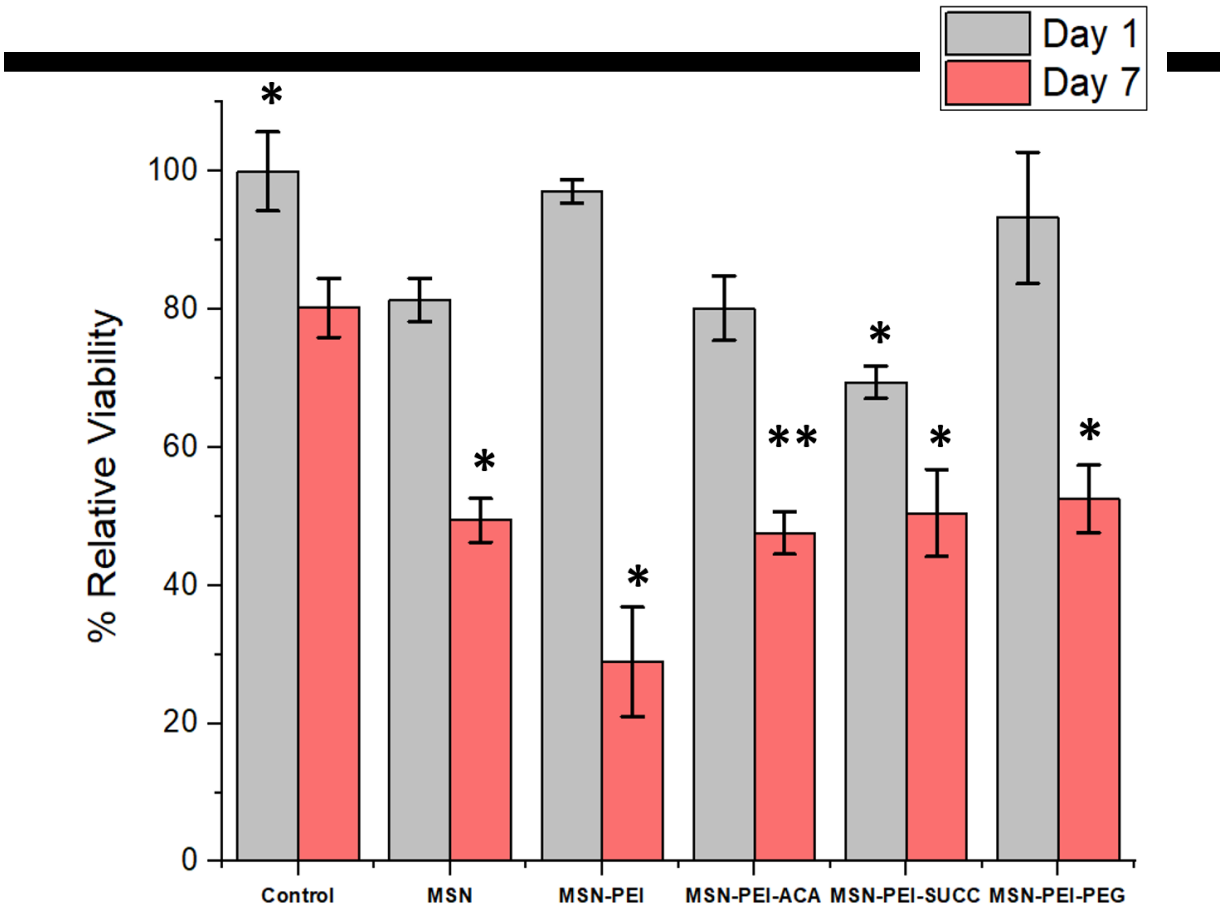

Figure 4.6) MSNs caused time-dependent cytotoxicity in NFC/GelMA composite matrix: Relative %viability of C2C12 cells (Initial cell concentration: 10^7cells/m) inside the photo-crosslinked NFC/GelMA (0.9% w/v, 4.5% w/v) composite matrix, incorporated with MSN-NH_2, MSN-PEI, MSN-PEI-PEG, MSN-PEI-ACA and MSN-PEI-SUCC (50µg/ml) on day 1 and day 7, based on the image analysis of the live/dead assay. Bar=mean±SEM; n=3. *, $p<0.05$; **, $p<0,01$.

4.7) Distribution of MSNs inside the NFC/GelMA Composite Matrix

TRITC-MSN-incorporated NFC/GelMA (0.9% w/v, 4.5% w/v) composite matrices with a nanoparticle concentration of 150 µg/ml were prepared, and imaged by using confocal microscopy as Z-stacks. The rendered images are given in **Figure 4.7**. Based on the results, TRITC-MSN-PEI-SUCC and TRITC-MSN-PEI-PEG showed a uniform dispersion within the NFC/GelMA composite matrix, whereas TRITC-MSN-PEI and TRITC-MSN-PEI-ACA was poorly dispersed. Therefore, TRITC-MSN-PEI-PEG and TRITC-MSN-PEI-SUCC was considered to help achieve a more uniform cellular internalization and dosage control.

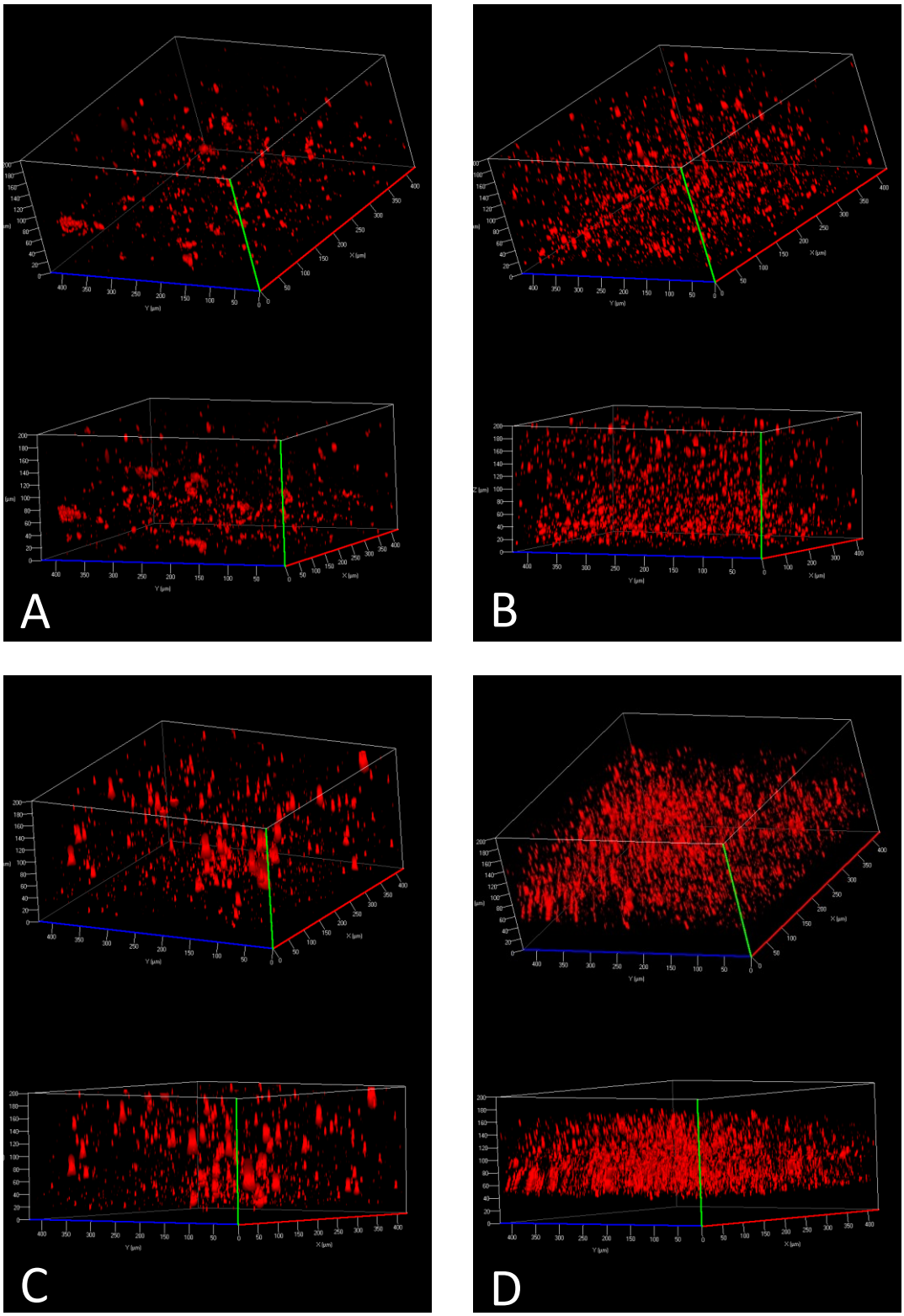

Figure 4.7) MSN distribution in the NFC/GelMA matrix: Z-stack confocal microscopy images of the NFC/GelMA (0.9% w/v, 4.5% w/v) composite matrices with an TRITC-MSN (Red) concentration of 150 µg/ml, acquired with Plan Achromat 20X objective (A: TRITC-MSN-PEI, B: TRITC-MSN-PEI-PEG, C: TRITC-MSN-PEI-ACA, D: TRITC-MSN-PEI-SUCC; z-stack size: 0.42x0.42x0.2 mm, XxYxZ axes).

4.8) TRITC-MSN-PEI-SUCC loaded with DiD showed Rapid Intracellular Drug Delivery Ability in NFC/GelMA Matrix

Based on its uniform distribution and low cytotoxicity inside the NFC/GelMA matrix on the previous experiments, MSN-PEI-SUCC was selected as the model nanoparticle to assess the intracellular drug delivery. DiD was used as a model hydrophobic drug for assessment of the intracellular drug delivery ability of MSN-PEI-SUCC.

TRITC-labelled MSN-PEI-SUCC incorporated cell-laden NFC/GelMA (0.9% w/v, 4.5% w/v) composite hydrogel was prepared with a nanoparticle concentration of 50 µg/ml. The live cells were then stained with calcein AM, and imaged as Z-stacks by using confocal microscopy. The fluorescence signals received from calcein AM, TRITC and DiD were depicted as neutral, blue and red respectively. However, during the imaging, the fluorescence signal received from TRITC-MSN-PEI-SUCC was weak. Therefore, the particles could be discerned only by means of the fluorescence emitted from DiD. Based on the confocal microscopy images, DiD-loaded TRITC-MSN-PEI-SUCC showed significant intracellular drug delivery ability starting from day 1, even before the onset of the cellular attachment. The intracellular drug delivery with the nanoparticles continued on day 3, and peaked on day 7 (**Figure 4.8**). On the other hand, TRITC-MSN-PEI-SUCC/DiD localized inside the cells as clusters.

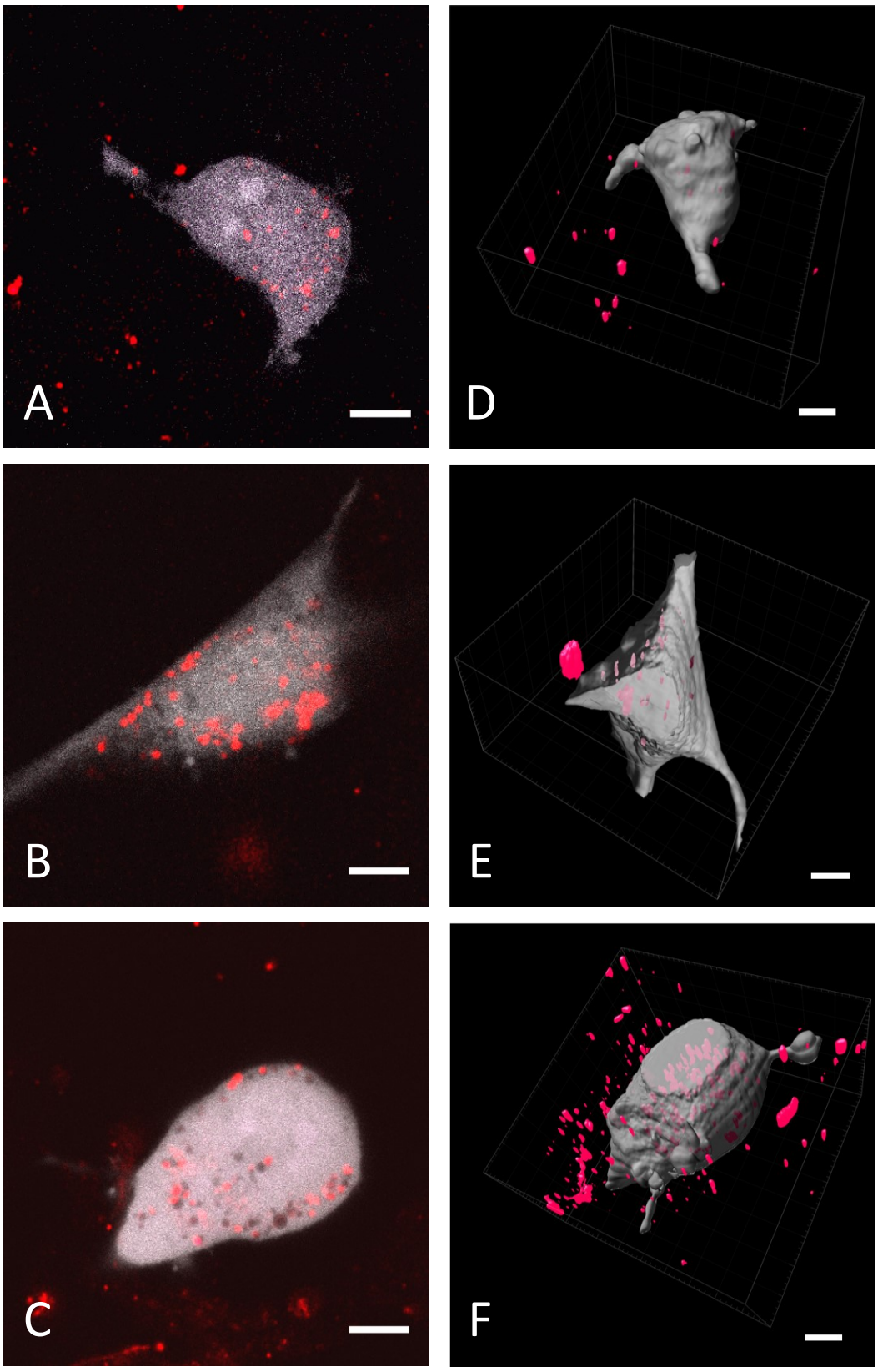

Figure 4.8) MSN-PEI-SUCC shows high intracellular drug delivery ability: 2D confocal microscopy images and rendered z-stacks of TRITC-labelled MSN-PEI-SUCC (Blue) loaded with DiD (Red) by C2C12 (Neutral) in cell-laden NFC/GelMA (0.9 w/v, 4.5 w/v) composite matrix on day 1 (A,D), day 3 (B,E), and day 7 (C,F) following the printing, acquired with 100X objective (Scale bar: 6 µm).

5) DISCUSSION

5.1) The Printability and the Mechanical Properties of the NFC/GelMA Composite Bioink

NFC/GelMA (0.9% w/v, 4.5% w/v) composite bioink showed excellent printability with 25G and 30G printing needles. In addition, encapsulation of cells at a high concentration (10^7 cells/ml) did not affect the printability significantly. In this regard, our results correlate with the previous studies, where concentrations as high as 9.6 million cells did not affect the mechanical properties of hydrogels (Hölzl et al., 2016).

In contrast to the previous research, no phase separation was observed during extrusion, when GelMA:NFC ratio was adjusted to be 5:1 (Xu et al., 2019). In addition, the structure maintained its shape without an extra step of Ca^{+2} stabilization after UV photo-crosslinking as suggested in the previous studies. However, the structural fidelity must be maintained not only after the photo-crosslinking, but also during the entire culture period. Following 60 seconds of photo-crosslinking with UV irradiation, the composite structures were incubated in cell media for 14 days. The decomposition immensely impacted the viability assays as staining of the dead cells with propidium iodide was not possible at thicknesses more than 0.8 mm, due to the diffusion limitations. The NFC/GelMA composite structures with 0.8 mm thickness started to decompose in the cell media already after 7 days. Even though 7 days of structural integrity of the printed scaffold was reported to be a success for regenerative medicine (Negrini et al., 2018), the observation of myoblast proliferation and myogenesis was impossible in such short period of time. Therefore, a different strategy to provide the 3D culture with nutritional compounds must be developed, rather than culturing it in liquid cell media, to prevent the matrix decomposition in the early stages of cell proliferation, and avail observation of myogenesis.

During the compression test, the sample ruptured during its transfer, and adhered to the measuring probe. Therefore, the compressive test must be repeated for more reliable data. However, based on the current measurement, the stiffness of NFC/GelMA (0.9% w/v, 4.5% w/v) after 60 seconds of UV irradiation was as high as 75 kPa, which is way too high than that of the native skeletal tissue (8-17 kPa) (Engler et al., 2006). Furthermore, the stiffness value cannot be tuned down to match such low value by decreasing the

photo-crosslinking, due to the aforementioned decomposition concerns at shorter durations of UV irradiation. Therefore, the developed NFC/GelMA might not be suitable for cultivation of myoblasts with the used concentrations in terms of the mechanical aspect of skeletal muscle niche. However, we suggest that NFC/GelMA (0.9% w/v, 4.5% w/v) can serve as a better bioink platform for stiffer tissues, such as cartilage and bone.

5.2) Viability of C2C12 Cells Incorporated into the NFC/GelMA Composite Matrix

The viability of the C2C12 cells inside the NFC/GelMA matrix was as low as 18.04±1.29% and 14.48±1.84% on day 1 and day 7, respectively. However, no other comparable study was found in the literature, where such 3D viability quantization for cell-laden photo-crosslinkable NFC/GelMA bioink was employed. The most relevant study was conducted by Shin et al. (2017), where they used ammonium persulfate (APS) and tetramethylethylenediamine (TEMED) as thermal crosslinking agents to crosslink GelMA (5% w/v) inside NFC (1% w/v), instead of a UV photo-crosslinking agent. Even though the authors stated that they achieved high viability with a concentration of NIH 3T3 cells as low as $1.5x10^6$ cells/ml, they did not perform any 3D quantization inside the gel matrix, and avoided giving a viability percentage. On another study conducted by Xu et al. (2019), the authors again seeded NIH 3T3 cells on top of an already UV-crosslinked NFC/GelMA (weight compositional ratio of 5:1). By conducting an MTT assay on 24^{th} hour following the cell seeding, they estimated the cell survival to be higher than 90%. However, such quantization still omits the effects of the shear forces during the 3D-printing and UV crosslinking, and does not answer the question of cell growth inside the composite matrix. In addition, it is already known that the cells behave differently in 2D and 3D cultures (Wong et al, 2015).

The low viability can be attributed to the shear forces during the 3D-printing. Nair et al. (2009) reported that, the cell viability in alginate bioinks decreased almost 40%, when the printing pressure was increased from 5 psi to 40 psi with 25G needle. Another reason for the low viability, related to the shear forces, can be the possible morphological damage exerted on the cells during their incorporation to the gel. Therefore, the rheologic properties of NFC/GelMA should be further investigated to have a better understanding of the possible negative effects of shear forces on cell viability.

UV irradiation might also be one of the factors affecting the viability. Yet, cytotoxicity caused by UVA (UV with wavelength 315-400 nm) is still controversial. Wong et al. (2015) reported that UVA exposure did not significantly affect the gene expression in human mesenchymal stem cells (hMSCs) growing in PEG hydrogel. However, they showed that the polymerization method, the change in the polymer network and free radicals had an important influence on gene expression. In addition, Kessler et al. (2017) reported that they achieved high viability with adipose-derived stem cells (ASCs) encapsulated in HyaMA (methacrylated hyaluronan)/GelMA composite hydrogels even after 5 minutes of UVA irradiation, where they used lithium phenyl-2,4,6-trimethylbenzoylphosphinate (LAP) as a photo-crosslinker. These studies suggest that the low viability in our study might be attributed to the NFC/GelMA network and the nature of the crosslinking or the photo-crosslinker. However, the viability might be improved by adding a free radical scavenger, such as ebselen (Miorelli et al., 2017), into the bioink to prevent hydroxylation of DNA caused by UV irradiation.

In addition to the adverse effects of UV irradiation, the composite NFC/GelMA matrix itself might not be suitable for cell growth considering the viability decreased on day 7 of the culture in comparison to that on day 1. Such results can be attributed to possible low porosity of the photo-crosslinked NFC/GelMA composite matrix and the dense fibre network. This hypothesis is also supported by the poor cellular attachment inside composite matrix even on day 7, as can be seen on **Figure 4.5.2**. Furthermore, a shorter photo-crosslinking time cannot be selected as the matrix decomposes inside the cell media with UV irradiation lower than 60 seconds.

These results indicate that the possible cytotoxicity caused by UV exposure might immensely limit the tunability and potential use of photo-crosslinkable NFC/GelMA composite bioinks in tissue engineering applications, which were reported by Xu (2019). Ultimately, to have a better understanding of the fibre network, the cellular attachment and mobility inside the composite matrix must be further investigated by using (e.g.) scanned electron microscopy (SEM) to assess the suitability of the material for cell growth.

5.3) MSN Cytotoxicity inside the Photo-crosslinked NFC/GelMA Composite Matrix

The addition of MSNs with a concentration of 50µg/ml caused low viability in a time-dependent manner. On day 1, the viability observed in the NFC/GelMA composite matrix incorporated with MSN-PEI was comparable to that of the control. Whereas, the lowest viability was achieved with MSN-PEI-SUCC conflicts with the previous study; where MSN-PEI caused significant cytotoxicity, and MSN-PEI-SUCC was not significantly cytotoxic in the 2D model (Paatero et al., 2017). However, contrarily on day 7, the lowest viability was observed with MSN-PEI, whereas higher viability was achieved with MSN-PEI-SUCC. Also, the viability achieved with MSN-NH_2, MSN-PEI-PEG, MSN-PEI-ACA and MSN-PEI-SUCC were similar on day 7. On the other hand, the low viability caused by MSN-PEI on day 7 comply with the previous studies, where MSN-PEI caused significant cytotoxicity in the 2D model (Paatero et al., 2017; Prabhakar et al., 2016). One interesting note was that viability achieved with MSN-NH_2 was significantly lower than that of the control on both day 1 and day 7 in contrast to the previous study, where MSN-NH_2 caused no significant toxicity in the 2D model (Prabhakar et al., 2016). Furthermore, the implement of MSNs in 3D cell cultures is a considerably new practice. Therefore, the MSN dosage in the NFC/GelMA matrix must be further optimized.

These results suggest that MSN-material interactions heavily impact MSN behaviour, and 2D viability assays for MSN cytotoxicity are not correlatable to 3D models. Therefore, the MSN-material interactions should be investigated thoroughly (e.g.) by using SEM to assess their potential use in tissue engineering applications. Furthermore, considering the drastic change of the viability between the day 1 and day 7, in addition to the slow cellular attachment and growth inside the composite matrix, the samples should be followed up more than 7 days. However, the samples partially decomposed inside the cell media due to their low thickness after day 7 and could no longer be imaged.

5.4) Intracellular Drug Delivery Ability and Distribution of TRITC-MSN-PEI-SUCC/DiD in the NFC/GelMA Composite Matrix

TRITC-MSN-SUCC/DiD showed high indtracellular drug delivery ability starting from day 1. The drug delivery ability of TRITC-MSN-PEI-SUCC might also be correlated to our cellular viability experiment, where MSN-PEI-SUCC showed high toxicity on day 1, and its toxicity was balanced on day 7 in a range similar to that of the other nanoparticles except MSN-PEI.

The results might be attributed to the higher availability and transport efficiency of MSN-PEI-SUCC within the matrix compared to the other MSNs. This hypothesis is supported by previous findings where negatively charged nanoparticles showed significantly higher translocation and transport efficiency in monolayer Caco-2 colon carcinoma cells, compared to positively charged nanoparticles (Bannunah et al., 2014). The availability of TRITC-MSN-SUCC is also supported by its uniform distribution inside the composite matrix. Desai (2016) showed that MSN-PEI-SUCC (300 nm) underwent the least amount of protein coating compared to MSN-PEI and MSN-PEI-PEG in serum containing media. They also demonstrated that MSN-PEI-SUCC maintained its negative surface charge after the incubation of the nanoparticles in serum containing media, whereas the zeta potential of MSN-PEI and MSN-PEI-PEG drastically lost their positive surface charge and approached to the neutral range. Based on this information, TRITC-MSN-SUCC could have preserved its intact surface properties also inside the NFC/GelMA (0.9 w/v, 4.5 w/v) matrix, suggesting that it is a promising drug delivery tool in 3D cell cultures. However, this hypothesis requires further justification.

On the other hand, the clustering of the TRITC-MSN-PEI-SUCC/DiD might be attributed to lysosomal co-localization. Prabhakar (2017) suggest that observation of the clusters indicate the entrapment of the nanoparticles inside the endosomes. Such findings can be caused by the large negative surface charge of TRITC-MSN-PEI-SUCC/DiD. These results comply with the previous studies, which suggest that negatively charged nanoparticles co-localize within the lysosomes, whereas positive surface charge induces endosomal escape of the nanoparticles (Yue et al., 2011). However, the effect of DiD loading on the nanoparticle fate inside the cells should not be omitted. According to Desai (2016), the hydrophobicity of DiD changed the hydrophilic nature of MSN-PEI, and thus it caused lysosomal co-localization after 24 hours, whereas MSN-PEI without DiD

followed a different path inside the cell. Therefore, the cargo delivery capability of TRITC-MSN-PEI-SUCC should further be investigated as the therapeutic potential of MSNs is dependent not only on their cellular internalization, but also on their drug release potential inside the cell.

6) CONCLUSION

The NFC/GelMA (0.9 w/v, 4.5 w/v) bioink has excellent printability and fidelity both before and after the photo-crosslinking. It shows sufficient structural integrity in cell media for at the least of 14 days, when printed at a thickness of 1.6 mm. However, at lower thickness values the gel decomposes inside the cell media starting from day 7. Such results suggest that better culture systems should be employed to maintain the structural integrity, rather than using conventional static culture methods in liquid cell media. In terms of biocompatibility, the NFC/GelMA composite bioink leaves room for improvement. After a culture period of 7 days, only a low viability (below 15%) was achieved when the C2C12 cells were incorporated with the composite matrix. In the light of the previous studies, such low viability and is hypothesized to be caused by the change in the fibre network and the cell environment after the photo-crosslinking. This hypothesis is also supported by the poor cellular attachment in the composite matrix. However, these results should be supported with SEM, both to investigate the porosity of the NFC/GelMA composite matrix and MSN- hydrogel interactions to assess its suitability as a potential scaffold material for tissue engineering. On the other hand, it shows way higher elastic moduli than that of skeletal muscle tissue. Therefore, it might be a better candidate as a bioink for cartilage or bone tissue engineering scaffold, rather than for skeletal muscle. Furthermore, MSN incorporation decreases the viability. Therefore, their dosage in 3D cultures must be further optimized. On the other hand, among the MSNs we used in our study, MSN-PEI-SUCC shows the most uniform distribution in the composite matrix. It also facilitates slightly higher viability compared to the other nanoparticles in the NFC/GelMA composite matrix, and shows rapid intracellular drug delivery ability. Such results are attributed to the high availability and transport efficiency of MSN-PEI-SUCC, possibly caused by the low level of surface interactions between the nanoparticles and the composite matrix. However, as suggested before, the interactions between the nanoparticles and the NFC/GelMA should be further investigated via SEM to support such a hypothesis.

7) ACKNOWLEDGEMENTS

This thesis work was conducted in Pharmaceutical Sciences Laboratory, Faculty of Science and Engineering at Åbo Akademi. I would like express my profound gratitude to my thesis supervisor Prof. Jessica Rosenholm of Pharmaceutical Sciences Laboratory, for making me feel warmly welcome to her laboratory first as an intern, and then as a Master's student. Prof. Rosenholm allowed me to work independently throughout my work, but she provided me with access to the research facilities and whatever expertise necessary. The door to her office has always been open to me, whenever I was in need of guidance. I would like to thank the members of BioNanoMaterials Group for their friendship and support. Particularly, I cannot thank enough to my thesis mentor Ph.D. student Ezgi Özliseli for allowing me to be a part of her projects without hesitation, and training me as a skilful researcher. She has always been willing to help me with my research, and give her precious support. Not only has she been a great teacher, but she also has been a dear friend. I would like to thank Didem Sen Karaman for her friendship and guidance with the mesoporous silica nanoparticles.

I would like to greatly thank Prof. Cecilia Sahlgren for agreeing to evaluate my thesis as the second reader. I wish to acknowledge my professors Diana Toivola and Pekka Hänninen for giving me the opportunity to be a part of Master's Programme in Biomedical Imaging and their valuable support. I sincerely acknowledge programme coordinators Joanna Pylvänäinen and Maritta Löytömäki and Turku Bioimaging family for their assistance. I, again, acknowledge Ezgi Özliseli and Åbo Akademi Laboratory of Wood and Paper Chemistry for supplying the nanofibrillated cellulose used in this study. I wish to thank Cell Imaging Core personnel for training and giving me access to the microscopes.

Figure 1, 1.2, 1.4, 1.6.b and **1.6.1** on this thesis was created with BioRender.com.

8) REFERENCES

Ahmed, E.M. 2015. Hydrogel: Preparation, characterization, and applications: A review. *J. Adv. Res.* 6:105–21. doi:10.1016/j.jare.2013.07.006.

Alexandrescu, L., K. Syverud, A. Gatti, and G. Chinga-Carrasco. 2013. Cytotoxicity tests of cellulose nanofibril-based structures. *Cellulose*. 20:1765–1775. doi:10.1007/s10570-013-9948-9.

Arab, W., S. Rauf, O. Al-Harbi, and C. Hauser. 2018. Novel Ultrashort Self-Assembling Peptide Bioinks for 3D Culture of Muscle Myoblast Cells. *Int. J. Bioprinting*. 4:1–13. doi:10.18063/ijb.v4i1.129.

Ávila, H.M., S. Schwarz, N. Rotter, and P. Gatenholm. 2016. 3D bioprinting of human chondrocyte-laden nanocellulose hydrogels for patient-specific auricular cartilage regeneration. *Bioprinting*. 1–2:22–35. doi:10.1016/j.bprint.2016.08.003.

Bacakova, L., J. Zarubova, M. Travnickova, J. Musilkova, J. Pajorova, P. Slepicka, N.S. Kasalkova, V. Svorcik, Z. Kolska, H. Motarjemi, and M. Molitor. 2018. Stem cells: their source, potency and use in regenerative therapies with focus on adipose-derived stem cells – a review. *Biotechnol. Adv.* 36:1111–1126. doi:10.1016/J.BIOTECHADV.2018.03.011.

Bannunah, A.M., D. Vllasaliu, J. Lord, and S. Stolnik. 2014. Mechanisms of nanoparticle internalization and transport across an intestinal epithelial cell model: Effect of size and surface charge. *Mol. Pharm.* 11:4363–4373. doi:10.1021/mp500439c.

Baumann, B., R. Wittig, and M. Lindén. 2017. Mesoporous silica nanoparticles in injectable hydrogels: Factors influencing cellular uptake and viability. *Nanoscale*. 9:12379–12390. doi:10.1039/c7nr02015e.

Belli, V., D. Guarnieri, M. Biondi, and P.A. Netti. 2017. Colloids and Surfaces B : Biointerfaces Dynamics of nanoparticle diffusion and uptake in three-dimensional cell cultures. *Colloids Surfaces B Biointerfaces*. 149:7–15. doi:10.1016/j.colsurfb.2016.09.046.

Buas, M.F., and T. Kadesch. 2010. Regulation of skeletal myogenesis by Notch. *Exp. Cell Res.* 316:3028–3033. doi:10.1016/j.yexcr.2010.05.002.

Chinga-Carrasco, G. 2011. Cellulose fibres, nanofibrils and microfibrils: The morphological sequence of MFC components from a plant physiology and fibre technology point of view. *Nanoscale Res. Lett.* 6:1–7. doi:10.1186/1556-276X-6-417.

Chithrani, B.D., and W.C.W. Chan. 2007. Elucidating the mechanism of cellular uptake and removal of protein-coated gold nanoparticles of different sizes and shapes. *Nano Lett.* 7:1542–1550. doi:10.1021/nl070363y.

Desai, D. 2016. Mesoporous silica nanoparticles as versatile intracellular drug delivery platform. Åbo Akademi University, Turku/Finland.

Desai, D., D. Sen Karaman, N. Prabhakar, S. Tadayon, A. Duchanoy, D.M. Toivola, S. Rajput, T. Näreoja, and J.M. Rosenholm. 2014. Design considerations for mesoporous silica nanoparticulate systems in facilitating biomedical applications. *Open Mater. Sci.* 1:16–43. doi:10.2478/mesbi-2014-0001.

El-Sherbiny, I., and M. Yacoub. 2013. Hydrogel scaffolds for tissue engineering: Progress and challenges. *Glob. Cardiol. Sci. Pract.* 2013:316–42. doi:10.5339/gcsp.2013.38.

Engler, A.J., S. Sen, H.L. Sweeney, and D.E. Discher. 2006. Matrix elasticity directs stem cell lineage specification. *Cell*. 126:677–89. doi:10.1016/j.cell.2006.06.044.

Enwere, E.K., E.C. LaCasse, N.J. Adam, and R.G. Korneluk. 2014. Role of the TWEAK-Fn14-cIAP1-NF-κB signaling axis in the regulation of myogenesis and muscle homeostasis. *Front. Immunol.* 5:1–14. doi:10.3389/fimmu.2014.00034.

Florczyk, S.J., M. Simon, D. Juba, P.S. Pine, S. Sarkar, D. Chen, P.J. Baker, S. Bodhak, A. Cardone, M.C. Brady, P. Bajcsy, and C.G. Simon. 2017. A Bioinformatics 3D Cellular Morphotyping Strategy for Assessing Biomaterial Scaffold Niches. *ACS Biomater. Sci. Eng.* 3:2302–2313. doi:10.1021/acsbiomaterials.7b00473.

Furth, E.M., and A. Atala. 2014.Tissue engineering: Future perspectives. In: Principles of Tissue Engineering (edited by Lanza R, Langer R, Vacanti J). Principles of Tissue Engineering. Elsevier. pp 83-104.

Hoffmann, F., M. Cornelius, J. Morell, and M. Fröba. 2006. Silica-based mesoporous organic-inorganic hybrid materials. *Angew. Chemie - Int. Ed.* 45:3216–3251. doi:10.1002/anie.200503075.

Hölzl, K., 7 S. Lin, L. Tytgat, S.Vlierberghe, L. Gu and A. Ovsianikov. 2016. Bioink properties before, during and after 3D bioprinting. *Biofabrication*. 8.

Hubbe, M.A., P. Tayeb, M. Joyce, P. Tyagi, M. Kehoe, K. Dimic-Misic, and L. Pal. 2017. Rheology of Nanocellulose-ric Aqueous Suspensions: A Review. *BioResources*. 12:9556–9661. doi:10.15376/biores.12.4.Hubbe.

Ingulli, E. 2010. Mechanism of cellular rejection in transplantation. *Pediatr. Nephrol.* 25:61–74. doi:10.1007/s00467-008-1020-x.

Iversen, T., T. Skotland, and K. Sandvig. 2011. Endocytosis and intracellular transport of nanoparticles : Present knowledge and need for. *Nano Today*. 6:176–185. doi:10.1016/j.nantod.2011.02.003.

Jiang, W., B.Y.S. Kim, J.T. Rutka, and W.C.W. Chan. 2008. Nanoparticle-mediated cellular response is size-dependent. *Nat. Nanotechnol.* 3:145–150. doi:10.1038/nnano.2008.30.

Jin, H., D.A. Heller, R. Sharma, and M.S. Strano. 2009. Size-dependent cellular uptake and expulsion of single-walled carbon nanotubes: Single particle tracking and a generic uptake model for nanoparticles. *ACS Nano*. 3:149–158. doi:10.1021/nn800532m.

Jokerst, J. V, T. Lobovkina, R.N. Zare, and S.S. Gambhir. 2011. Nanoparticle PEGylation for imaging and therapy. *Futur. Med.* 6:715–728. doi:10.2217/nnm.11.19.Nanoparticle.

Kessler, L., S. Gehrke, M. Winnefeld, B. Huber, E. Hoch, T. Walter, R. Wyrwa, M. Schnabelrauch, M. Schmidt, M. Kückelhaus, M. Lehnhardt, T. Hirsch, and F. Jacobsen. 2016. Methacrylated gelatin/hyaluronan-based hydrogels for soft tissue engineering. *J. Tissue Eng.* 8. doi:10.1177/2041731417744157.

Killian, M.L., L. Cavinatto, L.M. Galatz, and S. Thomopoulos. 2012. Recent advances in shoulder research. *Arthritis Res. Ther.* 14. doi:10.1186/ar3846.

Kim, C.O., S.J. Cho, and J.W. Park. 2003. Hyperbranching polymerization of aziridine on silica solid substrates leading to a surface of highly dense reactive amine groups. *J. Colloid Interface Sci.* 260:374–378. doi:10.1016/S0021-9797(03)00039-0.

Kim, D.Y., J.S. Kwon, J.H. Lee, L.M. Jin, J.H. Kim, and M.S. Kim. 2015. Effects of the Surface Charge of Stem Cell Membranes and DNA/Polyethyleneimine Nanocomplexes on Gene Transfection Efficiency. *J. Biomed. Nanotechnol.* 11:522–30. doi:10.1166/jbn.2015.2060.

Kim, T., M. Eltohamy, M. Kim, R.A. Perez, J. Kim, Y. Yun, J. Jang, E. Lee, J.C. Knowles, and H. Kim. 2014. Acta Biomaterialia Therapeutic foam scaffolds incorporating biopolymer-shelled mesoporous nanospheres with growth factors. *Acta Biomater.* 10:2612–2621. doi:10.1016/j.actbio.2014.02.005.

Kyle, S., Z.M. Jessop, A. Al-Sabah, and I.S. Whitaker. 2017. 'Printability'' of Candidate Biomaterials for Extrusion Based 3D Printing: State-of-the-Art.' *Adv. Healthc. Mater.* 6:1–16. doi:10.1002/adhm.201700264.

Laternser, S., H. Keller, O. Leupin, M. Rausch, U. Graf-hausner, and M. Rimann. 2018. A Novel Microplate 3D Bioprinting Platform for the Engineering of Muscle and Tendon Tissues. doi:10.1177/2472630318776594.

Laurén, P. 2018. Biomedical applications of nanofibrillar cellulose. University of Helsinki, Helsinki/Finland.

Lane, S.W., D.A. Williams, and F.M. Watt. 2014. Modulating the stem cell niche for tissue regeneration. *Nat. Biotechnol.* 32:795–803. doi:10.1038/nbt.2978.

Lee, J., D. Lilly, C. Doty, P. Podsiadlo, and N. Kotov. 2009. In vitro toxicity testing of nanoparticles in 3D cell culture. *Small*. 5:1213–1221. doi:10.1002/smll.200801788.

Leung, D.G., and K.R. Wagner. 2013. Therapeutic advances in muscular dystrophy. *Ann. Neurol.* 74:404–411. doi:10.1002/ana.23989.

Lin, J., W. Zhou, S. Han, V. Bunpetch, K. Zhao, C. Liu, Z. Yin, and H. Ouyang. 2018. Cell-material interactions in tendon tissue engineering. *Acta Biomater.* 70:1–11. doi:10.1016/j.actbio.2018.01.012.

Mamaeva, V., J.M. Rosenholm, L.T. Bate-Eya, L. Bergman, E. Peuhu, A. Duchanoy, L.E. Fortelius, S. Landor, D.M. Toivola, M. Lindén, and C. Sahlgren. 2011. Mesoporous silica nanoparticles as drug delivery systems for targeted inhibition of notch signaling in cancer. *Mol. Ther.* 19:1538–1546. doi:10.1038/mt.2011.105.

Merceron, T.K., and S. V Murphy. 2015. Hydrogels for 3D Bioprinting Applications. Elsevier Inc. 249-270 pp.

Miorelli, S.T., R.M. Rosa, D.J. Moura, J.C. Rocha, L.A. Carneiro Lobo, J.A. Pêgas Henriques, and J. Saffi. 2008. Antioxidant and anti-mutagenic effects of ebselen in yeast and in cultured mammalian V79 cells. *Mutagenesis*. 23:93–99. doi:10.1093/mutage/gem048.

Nair, K., M. Gandhi, S. Khalil, K.C. Yan, M. Marcolongo, K. Barbee, and W. Sun. 2009. Characterization of cell viability during bioprinting processes. *Biotechnol. J.* 4:1168–1177. doi:10.1002/biot.200900004.

Nichol, J.W., S.T. Koshy, H. Bae, C.M. Hwang, S. Yamanlar, and A. Khademhosseini. 2010. Biomaterials Cell-laden microengineered gelatin methacrylate hydrogels. *Biomaterials*. 31:5536–5544. doi:10.1016/j.biomaterials.2010.03.064.

O'Brien, F.J. 2011. Biomaterials & scaffolds for tissue engineering. *Mater. Today*. 14:88–95. doi:10.1016/S1369-7021(11)70058-X.

Paatero, I., E. Casals, R. Niemi, E. Özliseli, J.M. Rosenholm, and C. Sahlgren. 2017. Analyses in zebrafish embryos reveal that nanotoxicity profiles are dependent on surface-functionalization controlled penetrance of biological membranes. *Sci. Rep.* 7:8423. doi:10.1038/s41598-017-09312-z.

Prabhakar, N. 2017. Multimodal imaging probes and delivery systems for cancer nanomedicine. Åbo Akademi University, Turku/Finland.

Prabhakar, N., J. Zhang, D. Desai, E. Casals, T. Gulin-Sarfraz, T. Näreoja, J. Westermarck, and J.M. Rosenholm. 2016. Stimuli-responsive hybrid nanocarriers developed by controllable integration of hyperbranched PEI with mesoporous silica nanoparticles for sustained intracellular siRNA delivery. *Int. J. Nanomedicine*. 11:6591–6608. doi:10.2147/IJN.S120611.

Rejman J., V. Oberle, I.S. Zuhorn, and D. Hoekstra. 2004. Size-dependent internalization of particles via the pathways of clathrin- and caveolae-mediated endocytosis. *Biochem. J.* 377:159–169. doi:10.1042/bj20031253.

Romanazzo, S., G. Forte, M. Ebara, K. Uto, S. Pagliari, T. Aoyagi, E. Traversa, and A. Taniguchi. 2012. Substrate stiffness affects skeletal myoblast differentiation in vitro. *Sci. Technol. Adv. Mater.* 13. doi:10.1088/1468-6996/13/6/064211.

Rosenholm, J.M., A. Duchanoy, and M. Lindén. 2008. Hyperbranching surface polymerization as a tool for preferential functionalization of the outer surface of mesoporous silica. *Chem. Mater.* 20:1126–1133. doi:10.1021/cm7021328.

Rosenholm, J.M., J. Zhang, M. Linden, and C. Sahlgren. 2016. Mesoporous silica nanoparticles in tissue engineering – a perspective. *Futur. Med.* doi:https://doi.org/10.2217/nnm.15.212.

Rouwkema, J., S. Gibbs, M.P. Lutolf, I. Martin, G. Vunjak-Novakovic, and J. Malda. 2011. In vitro platforms for tissue engineering: implications for basic research and clinical translation. *J. Tissue Eng. Regen. Med.* 5:e164–e167. doi:10.1002/term.414.

Sayes, C.M., K.L. Reed, and D.B. Warheit. 2007. Assessing toxicology of fine and nanoparticles: Comparing in vitro measurements to in vivo pulmonary toxicity profiles. *Toxicol. Sci.* 97:163–180. doi:10.1093/toxsci/kfm018.

Sengupta, D., S.D. Waldman, and S. Li. 2014. From in vitro to in situ tissue engineering. *Ann. Biomed. Eng.* 42:1537–1545. doi:10.1007/s10439-014-1022-8.

Sheffield, C., K. Meyers, E. Johnson, and R. Rajachar. 2018. Application of Composite Hydrogels to Control Physical Properties in Tissue Engineering and Regenerative Medicine. *Gels*. 4:51. doi:10.3390/gels4020051.

Shin, S., S. Park, M. Park, E. Jeong, K. Na, H.J. Youn, and J. Hyun. 2017. Cellulose nanofibers for the enhancement of printability of low viscosity gelatin derivatives. *BioResources*. 12:2941–2954. doi:10.15376/biores.12.2.2941-2954.

Soares, C.P., V. Midlej, M.E.W. de Oliveira, M. Benchimol, M.L. Costa, and C. Mermelstein. 2012. 2D and 3D-organized cardiac cells shows differences in cellular morphology, adhesion junctions, presence of myofibrils and protein expression. *PLoS One*. 7. doi:10.1371/journal.pone.0038147.

Somers, S.M., A.A. Spector, D.J. DiGirolamo, and W.L. Grayson. 2017. Biophysical Stimulation for Engineering Functional Skeletal Muscle. *Tissue Eng. Part B Rev.* 23:362–372. doi:10.1089/ten.teb.2016.0444.

Stein, B.A., B.J. Melde, and R.C. Schroden. 2000. Hybrid Inorganic±Organic Mesoporous SilicatesÐNanoscopic Reactors Coming of Age. *Adv. Mater.* 1403–1419.

Vandenburgh, H., J. Shansky, F. Benesch-Lee, V. Barbata, J. Reid, L. Thorrez, R. Valentini, and G. Crawford. 2008. Drug-screening platform based on the contractility of tissue-engineered muscle. *Muscle and Nerve*. 37:438–447. doi:10.1002/mus.20931.

Vazquez, N.I., Z. Gonzalez, B. Ferrari, and Y. Castro. 2017. Synthesis of mesoporous silica nanoparticles by sol-gel as nanocontainer for future drug delivery applications. *Bol. la Soc. Esp. Ceram. y Vidr.* 56:139–145. doi:10.1016/j.bsecv.2017.03.002.

Vigodarzere, C.G., and S. Mantero. 2014. Skeletal muscle tissue engineering: strategies for volumetric constructs. *Front. Physiol.* 5:1–13. doi:10.3389/fphys.2014.00362.

Wang, Z., Z. Tian, F. Menard, and K. Kim. 2017. Comparative study of gelatin methacrylate hydrogels from different sources for biofabrication applications. *Biofabrication*. 9:44101. doi:10.1088/1758-5090/aa83cf.

Weishaupt, R., G. Siqueira, M. Schubert, P. Tingaut, K. Maniura-Weber, T. Zimmermann, L. Thöny-Meyer, G. Faccio, and J. Ihssen. 2015. TEMPO-Oxidized Nanofibrillated Cellulose as a High

Density Carrier for Bioactive Molecules. *Biomacromolecules*. 16:3640–3650. doi:10.1021/acs.biomac.5b01100.

Wong, D.Y., T. Ranganath, and A.M. Kasko. 2015. Low-dose, long-wave UV light does not affect gene expression of human mesenchymal stem cells. *PLoS One*. 10:1–21. doi:10.1371/journal.pone.0139307.

Xu, W. 2019. Three-dimensional printing of wood-derived biopolymers towards biomedical applications. Åbo Akademi University, Turku/Finland.

Xu, W., B.Z. Molino, F. Cheng, P.J. Molino, Z. Yue, D. Su, X. Wang, S. Willför, C. Xu, and G.G. Wallace. 2019. On Low-Concentration Inks Formulated by Nanocellulose Assisted with Gelatin Methacrylate (GelMA) for 3D Printing toward Wound Healing Application. *ACS Appl. Mater. Interfaces*. 11:8838–8848. doi:10.1021/acsami.8b21268.

Yang, P., S. Gai, and J. Lin. 2012. Functionalized mesoporous silica materials for controlled drug delivery. *R. Soc. Chem.* 41:3679–3698. doi:10.1039/c2cs15308d.

You, F., B.F. Eames, and X. Chen. 2017. Application of extrusion-based hydrogel bioprinting for cartilage tissue engineering. *Int. J. Mol. Sci.* 18:8–14. doi:10.3390/ijms18071597.

Yue, Z.G., W. Wei, P.P. Lv, H. Yue, L.Y. Wang, Z.G. Su, and G.H. Ma. 2011. Surface charge affects cellular uptake and intracellular trafficking of chitosan-based nanoparticles. *Biomacromolecules*. 12:2440–2446. doi:10.1021/bm101482r.

Zhang, C., F.G. Wu, P. Hu, and Z. Chen. 2014. Interaction of polyethylenimine with model cell membranes studied by linear and nonlinear spectroscopic techniques. *J. Phys. Chem. C*. 118:12195–12205. doi:10.1021/jp502383u.

Zhao, W., X. Jin, Y. Cong, Y. Liu, and J. Fu. 2013. Degradable natural polymer hydrogels for articular cartilage tissue engineering. *J. Chem. Technol. Biotechnol.* 88:327–339. doi:10.1002/jctb.3970.

Zorlutuna, P., N. Annabi, G. Camci-Unal, M. Nikkhah, J.M.Cha, J.W. Nichol, A. Manbachi, H. Bae, S. Chen and A. Khademhosseini. 2012. Microfabricated biomaterials for engineering 3D tissues. *Adv Mater*. 14:1782-1804. doi:10.1002/adma.201104631

Zschenker, O., T. Streichert, S. Hehlgans, and N. Cordes. 2012. Genome-wide gene expression analysis in cancer cells reveals 3D growth to affect ECM and processes associated with cell adhesion but not DNA repair. *PLoS One*. 7. doi:10.1371/journal.pone.0034279.

9) APPENDICES

Appendix I: User Manual Prepared for BIOBOTS Bioprinter

Switching on the Instrument:

-Switch on the computer
-Switch on the pump by pushing the red knob
-Switch on Biobots by clicking the button
-Open "Command prompt"
-Type the following command "**cd Desktop/bioprint-devel-master/bioprint-devel-master/bioprint**" and press Enter
-Type "python run" and press Enter, wait until the command works
-Open the Chrome Browser
-Navigate to "bioprint" page
-Login with the saved credentials
-Click "Connect" and wait until the printer is connected
-Connect the syringe to the air hose, insert inside the extruder and tighten the extruder knob.

Calibration:

-Home all axes (The order does not matter)
-Navigate to "Select Well Plate" and select your desired type of well plate
-Then click Select Well Plate, the extruder will move onto the well plate
-Adjust the Z plane by moving it upwards by 10 mm 2-3 times. Then switch to 1mm and keep elevating the plane until the needle tip approaches to the well plate surface. When in close proximity with the plate, switch to 0,1 mm and adjust the needle so as it almost touches the plate surface
-Once done, navigate to the control panel (right side of the screen), click "Update" and then "Calibrate". The printer will switch to the second extruder.
-If using both extruders or the second extruder, repeat the Z plane calibration for the second extruder as well.
-Once calibrated, home the Z plane.

-Adjust the printing pressure. Start by decreasing the pressure all the way. Click "Extrude" and increase the pressure slowly until you see a droplet on the needle tip. Click "Stop". Repeat the same steps for the second extruder if necessary.

-Check if the nozzle is calibrated properly by clicking "Go" on the control panel.

-The printer is now ready for printing.

Appendix II: List of the fluorophores used in the study and their excitation-emission maxima

Name of the Fluorophore	Excitation Max (nm)	Emission Max (nm)
TRITC	555	580
DiD	644	665
Propidium Iodide	493	636
Calcein AM	494	517